# CATHODOLUMINESCENCE DEGRADATION AND SURFACE CHARACTERIZATION OF $SrGa_2S_4:Ce^{3+}$ POWDER AND THIN FILMS

by

Pulane Adelaide Moleme

*A dissertation presented in fulfillment of the requirements for the degree*

MAGISTER SCIENTIAE

*in the*

**Faculty of Natural and Agricultural Sciences**

**Department of Physics**

*at the*

**University of the Free State**

**Republic of South Africa**

**Study Leader: Prof. O M Ntwaeaborwa**

**Co-Study Leader: Prof. H C Swart**

*May 2011*

**Dedicated to the memory of my late father**

**Jacob Moleme**

**(1935-2004)**

*‘‘Education or school does not equip us with abilities, instead, we are born with a horde of abilities. The school or education is there to identify and release the abilities we already possess’’*

**Acknowledgements**

I thank the Lord our God for the opportunity to undertake this study and for His Grace, without which this study would not have been possible.

I would take this opportunity to thank all who assisted me during the course of the research and with the preparation of this thesis. In particular, my special thanks are due to:

- My supervisor, Prof. O.M. Ntwaeaborwa, for his dedication, support, patience and understanding.

- My co-supervisor, Prof. H.C. Swart, for his valuable knowledge, esteemed guidance and countless help.

- Ulrich Buttner for his guidance and assistance in growing thin films at Stellenbosch University.

- South African National Research Foundation (NRF) and the University of the Free State (UFS) for financial support.

- The academic and non-academic staff of the UFS-Physics Department, all post-graduate students and the fellow research students for their constant support. In particular, I would like to thank Dr Shreyas S. Pitale for fruitful discussions on CL and XPS data of the powder and Dr Patrick Nsimama for helping during the preparation of the films by the pulsed laser deposition technique.

- My family for moral support, my mother and my beautiful children for understanding and exercising patience during the course of my work.

- The love of my life, Emmanuel.

- Finally, my outmost thanks to His Grace Dr. B. E. Lekganyane.

## ABSTRACT

The structure, morphology and luminescent properties of commercial $SrGa_2S_4:Ce^{3+}$ phosphor powder and thin films were investigated. The phosphor shows bright blue under ultraviolet (UV) excitation. Measurements were carried out using various characterization techniques such as X-ray diffraction (XRD), scanning electron microcopy (SEM) and X-ray energy dispersive spectroscopy (EDS). The XRD data were collected using a D8 advance powder X-ray diffractometer with CuKα radiation. Morphology and elemental composition were done using Shimadzu Super Scan SSX-550 coupled with EDS. Photoluminescence (PL) data were collected using Varian Cary Eclipse Fluorescence Spectrophotometer with a monochromatized Xenon lamp (60-75 W) as excitation source and measurements were carried out in air at room temperature, and cathodoluminescence (CL) data were collected with S2000 Ocean Optics Spectrometer. The absorption spectra were recorded using Perkin Elmer Lambda 950 UV-VIS spectrometer. The same characterization tools were used to characterize the thin films.

XRD data confirmed the orthorhombic structure of $SrGa_2S_4$ that was consistent with the standard JCPDS file no. (77-1189). The SEM images of the $SrGa_2S_4:Ce^{3+}$ powder showed particles with irregular shapes and EDS detected presence of the major elements. Both PL and CL showed the broad emission peaks around 444 nm and 485 nm which are due to $Ce^{3+}$ radiative transitions (5d $(T_{2g}) \rightarrow 4f\ (^2F_{5/2})$ and 5d $(T_{2g}) \rightarrow 4f\ (^2F_{7/2})$).

Cathodoluminescent ageing characteristics of the $SrGa_2S_4:Ce^{3+}$ powder and thin films under prolonged electron beam bombardment were studied and presented. The cathodoluminescent intensity with increasing Coulomb loading was observed to degrade under different primary electron beam voltages for the powder. Auger electron spectroscopy (AES) and X-ray photoelectron spectroscopy (XPS) were used to monitor the surface chemical changes both during electron beam bombardment and after the degradation process. Auger peak to peak heights monitored during the ageing process suggest a decrease in S and C Auger peak intensity and an initial increase in oxygen concentration on the surface. XPS results indicate the formation of an SrO overlayer due to electron stimulated surface chemical reactions (ESSCRs).

For preparation of films, silicon (Si) (100) substrates were used. A pellet was prepared from the standard $SrGa_2S_4:Ce^{3+}$ powder. The Lambda Physik EMG 203 MSC 309 nm XeCl excimer laser was used to grow the films. The films growth was carried out in a chamber which was first evacuated to a base pressure of $8 \times 10^{-5}$ mbar before backfilling to pressures of $1.0 \times 10^{-2}$ mbar Ar and $1.0 \times 10^{-2}$ mbar $O_2$, where Ar and $O_2$ were used as cross pulse gases. The films were deposited at different substrate temperatures ranging from 400°C to 600°C with 28 800 and 57 600 pulses respectively. The laser beam was operated at 8 Hz repetitive rate. The substrate temperature, number of pulses and the working pressure are the parameters that were varied during the preparation of the thin films.

A highly crystalline $SrGa_2S_4$ layer was obtained at the growth temperature of 400°C. XRD patterns also showed that the properties of the films were sensitive to substrate temperature. PL and CL spectra were characterized by a broad band that can be fitted by two Gaussian peaks according to the two $Ce^{3+}$ radiative transitions. At high substrate temperature a shift to $Ce^{3+}$ emission in SrS occurred as well as in Ar atmosphere for both UV and high energy electrons excitation. The atomic force microscopy (AFM) images before annealing exhibited smooth surface at low substrate temperature, which became rough at high substrate temperature and after annealing in vacuum at 700°C temperature. Non-uniformity in particles (big and small) of the films and smooth films were observed from the SEM images.

**Keywords:** $SrGa_2S_4:Ce^{3+}$, PL, CL, electron degradation, PRCLA, SEM, AFM, AES and XPS.

**ACRONYMS**

PL - Photoluminescence

CL - Cathodoluminescence

SEM - Scanning electron microscopy

EDS - Energy dispersive spectroscopy

XRD - X-ray diffraction

AFM - Atomic force microscopy

AES - Auger electron spectroscopy

APPHs - Auger peak-to-peak heights

XPS - X-ray photoelectron spectroscopy

PRCLA - Pulsed reactive cross laser ablation

XeCl - Xenon chloride

## TABLE OF CONTENTS

Title page i
Dedication ii
Acknowledgements iii
Abstract iv
Keywords + Acronyms v
List of figures ix
List of tables xii

## CHAPTER 1: Background information

Introduction
1.1 Phosphors 2
1.2 Classification of phosphors 2
1.3 Application of phosphors 3
1.3.1 Light source material-fluorescent lamp 3
1.3.2 Display devices-cathode ray tubes 4
1.3.3 Other applications of phosphors 6
1.4 Light emission by phosphors 6
1.4.1 Phosphorescence and fluorescence processes 7
1.4.2 Mechanism of luminescence 7
1.4.3 Main processes of luminescence 8
1.5 Rare-earth luminescence 11
1.5.1 $Ce^{3+}$ luminescence 11
1.6 Ternary sulfide phosphors and CL properties 12
1.7 Origin of the problem 13
1.8 Study Objectives 14
1.9 Thesis layout and experimental approach 14
References 16

## CHAPTER 2: Theory of Research Techniques (Principle of Operation)

Introduction
2.1 Pulsed Laser Deposition (PLD) 20

2.2 PRCLA (Pulsed Reactive Cross-Beam Laser Ablation) 20
2.3 Photoluminescence (PL) Spectroscopy 23
2.4 UV-Visible Spectrophotometery 24
2.5 X-Ray diffraction (XRD) 27
2.6 Scanning Electron Microscopy (SEM) 28
2.7 Atomic Force Microscopy (AFM) 31
2.8 Auger Electron Spectroscopy (AES) 32
2.9 Cathodoluminescence (CL) Spectroscopy 33
2.10X-ray Photoelectron Spectroscopy (XPS) 34
References 36

**CHAPTER 3: Structure, morphology and luminescent properties of $SrGa_2S_4:Ce^{3+}$ powder**

Introduction
3.1 Experimental procedure 39
3.2 Results and discussions 39
3.2.1 XRD and SEM/EDS 39
3.2.2 PL and CL 42
3.2.3 UV-Visible absorption 44
3.3 Conclusion 44
References 45

**CHAPTER 4: Cathodoluminescence degradation of $SrGa_2S_4:Ce^{3+}$ powder**

Introduction
4.1 Experimental procedure 47
4.2 Results and discussions 47
4.2.1 Residual gas analysis 47
4.2.2 CL intensity degradation 49
4.2.3 XPS analysis 55
4.3 Conclusion 57
References 58

**CHAPTER 5: $SrGa_2S_4:Ce^{3+}$ thin films growth, structure, morphology, topography and luminescent properties**

Introduction

5.1 Experimental procedure 60

5.2 Results and discussions 60

5.2.1 XRD 60

5.2.2 Elemental composition and particle morphology 62

5.2.3 Surface topography 63

5.2.4 Photoluminescence properties 64

5.2.5 Cathodoluminescence properties 66

5.3 Conclusion 67

References 68

**CHAPTER 6: Cathodoluminescence degradation of $SrGa_2S_4:Ce^{3+}$ thin films**

Introduction

6.1 Experimental procedure 70

6.2 Results and discussions 70

6.2.1 CL intensity degradation 70

6.2.2 XPS analysis 74

6.3 Conclusion 76

References 77

**CHAPTER 7: Summary and Conclusion**

Introduction

7.1 Thesis summary 79

7.2 Future work 81

References 82

## List of Figures


**Fig. 1.1 (a)** A typical fluorescent tube ..... 3

**Fig. 1.1 (b)** Different types of fluorescent lamps ..... 3

**Fig. 1.2 (a)** Typical cathode ray tube (CRT) used in televisions and computer display ..... 4

**Fig. 1.2 (b)** A schematic diagram showing basic components of CRT ..... 4

**Fig. 1.2 (c)** An old computer monitor ..... 4

**Fig.1.3** A schematic diagram of a Field Emission Display (FEDs) ..... 5

**Fig. 1.4 (a)** A drawing of an X-ray storage phosphor ..... 6

**Fig. 1.4 (b)** A drawing of a watch with luminescent paint pigment applied on it ..... 6

**Fig. 1.5 (a)** A schematic illustration of a configurational coordinate model ..... 8

**Fig. 1.5 (b)** A schematic diagram of energy bands showing transformation of excitation energy through radiative and non-radiative routes ..... 8

**Fig. 1.6** Different processes in luminescence and nature of transitions involved ..... 10

**Fig. 2.1** A schematic diagram of a typical laser deposition set-up ..... 20

**Fig. 2.2** A schematic diagram of a pulsed reactive cross laser ablation set-up ..... 21

**Fig. 2.3** The Pulsed Laser Deposition machine at Stellenbosch University, Physics department ..... 22

**Fig. 2.4 (a)** A schematic diagram showing the main elements for measuring photoluminescence spectra ..... 23

**Fig. 2.4 (b)** The Cary Eclipse Fluorescence Spectrophotometer at the University of the Free State, Physics department ..... 24

**Fig. 2.5 (a)** A schematic diagram of a single-beam spectrophotometer ..... 25

**Fig. 2.5 (b)** A schematic diagram of a double-beam spectrophotometer ..... 26

**Fig. 2.5 (c)** The Perkin Elmer Lambda 950 UV-VIS Spectrometer at the University of the Free State, Physics department ..... 26

**Fig. 2.6 (a)** A schematic diagram of a diffractometer system ..... 27

**Fig. 2.6 (b)** The D8 Advanced AXS GmbH X-ray diffractometer at the University of the Free State, Physics department ..... 28

**Fig. 2.7 (a)** A schematic diagram of a Scanning Electron Microscopy ..... 29

**Fig. 2.7 (b)** The Shumadzu Superscan SSX-550 SEM at the University of the Free State, Microbiology department ..... 30

**Fig. 2.7 (c)** The PHI 700 Auger Nanoprobe SEM unit at the University of the Free State, Physics department ..... 30
**Fig. 2.8 (a)** A simplified layout of Atomic Force Microscopy ..... 31
**Fig. 2.8 (b)** The Atomic Force Microscopy machine at the University of the Free State, Physics department ..... 32
**Fig. 2.9** The PHI model 549 Auger Electron Spectroscopy unit coupled with CL unit at the University of the Free State, Physics department ..... 33
**Fig. 2.10** The PHI 5000 XPS Versaprobe (monochromatic AlKα lines) machine at the University of the Free State, Physics department ..... 35
**Fig. 3.1** An X-ray diffraction pattern of the $SrGa_2S_4$ host lattice ..... 40
**Fig. 3.2 (a-c)** SEM images at different magnifications ..... 42
**Fig. 3.2 (d)** Energy Dispersive spectroscopy spectrum of $SrGa_2S_4:Ce^{3+}$ ..... 42
**Fig. 3.3 (a)** PL emission and excitation spectra of $SrGa_2S_4:Ce^{3+}$ powder ..... 43
**Fig. 3.3 (b)** Cerium ($Ce^{3+}$ ion) energy levels diagram ..... 43
**Fig. 3.3 (c)** CL emission spectrum of the $SrGa_2S_4:Ce^{3+}$ powder recorded at a pressure of 1.3 x $10^{-8}$ Torr (2keV) ..... 43
**Fig. 3.4** Optical absorption spectrum of $SrGa_2S_4:Ce^{3+}$ powder ..... 44
**Fig. 4.1 (a)** RGA taken before degradation with the beam on and off at a pressure of 1.3 x $10^{-8}$ Torr ..... 48
**Fig. 4.1 (b)** RGA taken before degradation with the beam on and off at $O_2$ pressure of 1.0 x $10^{-6}$ Torr ..... 48
**Fig. 4.1 (c)** RGA taken after degradation with the beam on at 1.3 x $10^{-8}$ Torr and 7.5 x $10^{-7}$ Torr $O_2$ ..... 48
**Fig. 4.2 (a)** AES spectrum of $SrGa_2S_4:Ce^{3+}$ powder recorded before and after ageing ..... 50
**Fig. 4.2 (b)** APPHs as a function of Coulomb loading recorded at 7.5 x $10^{-7}$ Torr $O_2$ ..... 50
**Fig. 4.3 (a)** CL emission of $SrGa_2S_4:Ce^{3+}$ powder recorded before and after ageing ..... 51
**Fig. 4.3 (b)** Normalised CL intensity as a function of electron dose of $SrGa_2S_4:Ce^{3+}$ powder at various oxygen pressures ..... 51
**Fig. 4.4 (a)** Ageing characteristics at various accelerating voltage degraded at a background pressure of 1.3 x $10^{-8}$ Torr ..... 52
**Fig. 4.4 (b)** Auger profile of $O_2$ recorded before and after ageing with 1.5 and 2.5 kV electron beam voltage at 1.3 x $10^{-8}$ Torr pressure ..... 52

**Fig. 4.4 (c)** Linear fits for the $SrGa_2S_4:Ce^{3+}$ powder at 1.5 and 2.5 kV electron beam voltage ..... 52

**Fig. 4.5 (a-f)** XPS high resolution scans and fitting results for undegraded and degraded region of $SrGa_2S_4:Ce^{3+}$ powder ..... 55

**Fig. 4.6** Illustration of possible chemical reactions taking place on the surface according to the ESSCR ..... 56

**Fig. 5.1 (a-c)** XRD patterns of the $SrGa_2S_4:Ce^{3+}$ films deposited at different parameters ..... 61

**Fig. 5.2 (a)** SEM micrograph of the $SrGa_2S_4:Ce^{3+}$ film deposited at 400$^oC$ ..... 62

**Fig. 5.2 (b)** Auger survey spectrum of the $SrGa_2S_4:Ce^{3+}$ film deposited at 400$^oC$ ..... 62

**Fig. 5.3 (a-c)** AFM images of the unannealed $SrGa_2S_4:Ce^{3+}$ films deposited at 400$^oC$, 500 $^oC$ and 600 $^oC$ ..... 63

**Fig. 5.3 (d-f)** AFM images of the $SrGa_2S_4:Ce^{3+}$ films annealed in vacuum at 700 $^oC$ ..... 63

**Fig. 5.4 (a-c)** PL emission spectra of the $SrGa_2S_4:Ce^{3+}$ films deposited at different parameters ..... 64

**Fig. 5.5 (a-c)** Unannealed and annealed PL emission spectra of the $SrGa_2S_4:Ce^{3+}$ films prepared at 400$^oC$, 500$^oC$ and 600$^oC$ ..... 65

**Fig. 5.6 (a-c)** CL emission spectra of the $SrGa_2S_4:Ce^{3+}$ films deposited at different parameters ..... 66

**Fig. 6.1 (a)** Auger spectra (before and after degradation) of the $SrGa_2S_4:Ce^{3+}$ film deposited at $T_{substrate}$ = 400$^oC$ with degradation performed at a pressure of 1.0 x $10^{-6}$ Torr $O_2$ ..... 71

**Fig. 6.1 (b)** APPHs and CL intensity as a function of electron dose spectra of the $SrGa_2S_4:Ce^{3+}$ film deposited at 400$^oC$ (1.0 x $10^{-6}$ Torr $O_2$) ..... 71

**Fig. 6.2** CL intensity as a function of wavelength spectra (before and after degradation) of the $SrGa_2S_4:Ce^{3+}$ film deposited at 400$^oC$ and 600 $^oC$ substrate temperatures degraded in the background pressure of 1.0 x $10^{-6}$ Torr $O_2$ ..... 72

**Fig. 6.3 (a)** Normalised CL intensity as a function of electron dose of the $SrGa_2S_4:Ce^{3+}$ films deposited at $T_{substrate}$ = 400$^oC$ and $T_{substrate}$ = 600 $^oC$ - degraded in the backround pressure of 1.0 x $10^{-6}$ Torr $O_2$ ..... 73

**Fig. 6.3 (b)** Normalised CL intensity as a function of electron dose of the $SrGa_2S_4:Ce^{3+}$ films deposited at $T_{substrate}$ = 400$^oC$ and $T_{substrate}$ = 600 $^oC$ – degraded in the backround pressure of 7.8 x $10^{-9}$ Torr ..... 73

**Fig. 6.4** CL intensity as a function of wavelength of the $SrGa_2S_4:Ce^{3+}$ film deposited at $T_{substrate}$ = 400°C recorded at various accelerating voltage ..... 61

**Fig. 6.5** XPS survey spectra (undegraded and degraded spots) of the $SrGa_2S_4:Ce^{3+}$ film deposited at $T_{substrate}$ = 600°C ..... 74

**Fig. 6.6** XPS high resolution scans and fitting results of undegraded and degraded regions of $SrGa_2S_4:Ce^{3+}$ film deposited at $T_{substrate}$ = 600°C ..... 75

## List of Tables

**Table 3.1** Crystallographic data for SrGa2S4 lattice ..... 40

**Table 3.2** h k l planes and d-spacings (calculated and theoretical values) ..... 41

**Table 4.1 (a)** CL degradation curves life-times at various oxygen pressures ..... 53

**Table 4.1 (b)** CL degradation curves life-times at different accelerating voltage ..... 53

# CHAPTER 1

# BACKROUND INFORMATION

## Introduction

*This chapter presents a unified picture and interpretations of the luminescence and related phenomena and the diversified areas of application of luminescent materials (phosphors). The emphasis is on setting forth a physical description, which can be used to obtain a qualitative understanding rather than on detailed mathematical analyses. Such analyses are by no means ignored, and references to them are provided in the chapter wherever necessary.*

## 1.1 Phosphors

A phosphor is a chemical substance that emits light (red, green and blue) when subjected to electromagnetic radiation (electrons, photons, etc.). Generally, a phosphor consists of a host lattice and a luminescent centre, often called an 'activator' or a 'dopant'. Activators are impurities introduced intentionally in a host lattice to serve as luminescent (light emitting) centers. In general the host needs to be transparent to the radiation source with which it is excited. One example of a phosphor is ZnS:Cu or ZnS:Cu,Au,Al, where ZnS is the host lattice and Cu is an activator. If more than one activator is used, additional activators (e.g. Au and Al) are called co-activators or co-dopants.

## 1.2 Classification of phosphors

Phosphors can be classified into two types namely oxides (ZnO, $Y_2O_3$, $SiO_2$) and sulfides (ZnS, CdS, CaS, SrS). Usually, most of these phosphors are doped with rare-earth elements such as $Eu^{3+}$, $Tb^{3+}$, $Ce^{3+}$ and $Pr^{3+}$ or metal ions such as Cu, Al, Ag, Cl and Au. In addition, phosphors can be classified according to the manner in which they emit light. For example, light emission can be a result of exciton recombination in the bandgap (no doping required) or atomic transition where a dopant is responsible for the emission. Light emission in phosphors such as ZnO and PbS with relatively smaller bandgap is due to excitonic recombination and this phosphors can be classified as bandgap transition phosphors, whereas phosphors such as $Y_2O_3$:RE (RE = $Eu^{3+}$, $Ce^{3+}$,$Tb^{3+}$. Etc) can be classified as atomic (dopant) transition phosphors because light emission in these phosphors is due to transitions taking place in the dopant.

Phosphors can be found in two forms, namely powders and thin films. In both powder and thin film forms, phosphors can be used in devices that emit light by a cathodoluminescent (CL) process. That is, emission of light when a phosphor is excited by high energy beam of electrons. Therefore, the choice of phosphors satisfying the CL properties becomes very important. In this study, CL studies on a rare-earth ternary alkaline earth sulfide ($SrGa_2S_4$:$Ce^{3+}$) were performed for application in field emission displays (FEDs). Detailed discussion is presented in the following chapters.

## 1.3 Applications of Phosphors

Typically, phosphors are applied in light source materials represented by fluorescent lamps and display devices represented by cathode ray tubes. Other applications include detectors represented by X-rays and scintillators as well as applications in simple luminous paints where phosphors with long persistent phosphorescence are used [1].

### 1.3.1 Light source materials - fluorescent lamp

Light sources extend life activities from dark to comfortably illuminated rooms [2]. One of the examples is fluorescent lamp. A fluorescent lamp has no filament running through it. Instead, it has cathodes (coiled tungsten filaments coated with an electron-emitting substance) at each end of the fluorescent tube. A typical fluorescent tube is filled with inert gas and a small amount of mercury that creates vapour. Ultraviolet radiation is produced as electrons from the cathodes knock mercury electrons out of their natural orbit. Some of the displaced electrons settle back into orbit, throwing off the excess energy absorbed in the collision. Almost all of this energy is in the form of ultraviolet radiation.

The inside of the tube has a phosphor lining which when collide with ultraviolet radiation gives off visible light. The phosphors have the unique ability to lengthen UV wavelengths to a visible portion of the spectrum. In other words, the phosphors are excited to fluorescence by bursts of UV energy [3]. Shown in Fig. 1.1 (a) is a picture illustrating a typical fluorescent tube and (b) the fluorescent lamps used by humans in their daily lives.

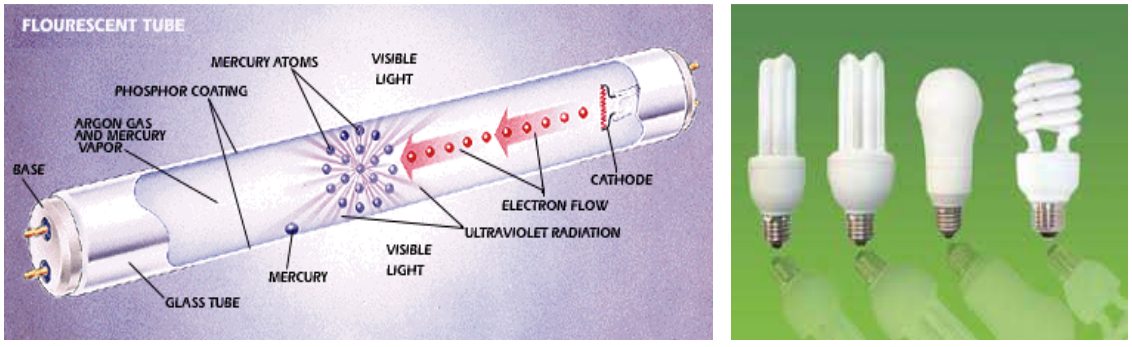


(a) (b)

**Fig. 1.1 (a)** A typical fluorescent tube [3] and **(b)** Different types of fluorescent lamps [4]

### 1.3.2 Display devices – Cathode ray tubes (CRTs)

Phosphor screens are currently in wide use as display devices and they also serve as the interface between information stored in electrons and humans [2]. CRTs are almost universally used phosphor screens in colour televisions and still dominate in the display monitors of desktop computers. Fig. 1.2 (a) shows the typical CRT used in conventional televisions and computer display, (b) is the schematic diagram showing the basic components of CRTs and (c) is the typical computer monitor used in the past.

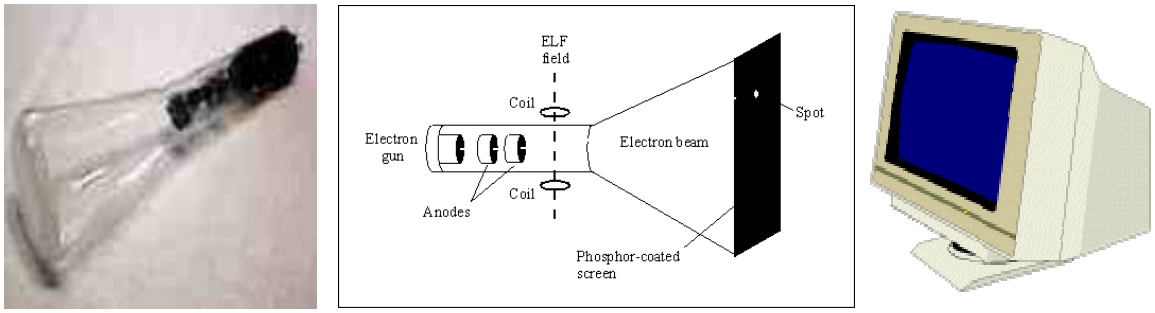


(a) (b) (c)

**Fig. 1.2 (a)** Typical CRT used in televisions or computer display, **(b)**, Schematic diagram showing basic components of CRT and **(c)** Old computer monitor [5, 6, 7].

A cathode ray tube (CRT) is a specialized vacuum tube in which images are produced when electron beam strikes a phosphorescent/fluorescent surface. It consists of several basic components as shown in Fig. 1.2 (b). The electron gun generates a narrow beam of electrons and the anode accelerates the electrons. Deflecting coils produce an extremely low frequency electromagnetic field that allows for constant adjustment of the direction of the electron beam and the intensity of the beam can be varied. The electron beam produces a tiny, bright visible spot when it strikes the phosphor coated screen.

To produce an image on the screen, complex signals are applied to the deflecting coils and the apparatus that controls the intensity of the electron beam. This causes the spot to race across the screen from right to left, and from top to bottom, in a sequence of horizontal lines called the raster. As viewed from the front of the CRT, the spot moves in a pattern similar to the way your eyes move when you read a single-column page of text. The scanning takes place at such a rapid rate that your eyes sees a constant image over the entire screen [5].

CRTs are obviously not suitable for laptop PCs, because of bulk and weight, where currently liquid crystal displays (LCDs) are the systems of choice [8]. However, flat panel display such as field emission displays (FEDs) encompass a growing number of technologies enabling video display that are much thinner and lighter than traditional television and video display that use cathode ray tube [9]. FED is one type of the flat panel display that is believed to poses a threat to LCDs' dominance in the emissive panel display arena. It capitalizes on the well-established cathode-anode phosphor technology built into full-sized cathode ray tubes, and uses that in combination with the dot matrix cellular construction of LCDs. Instead of using a single bulky tube, FEDs use tiny ''mini tubes'' for each pixel and the display can be build in approximately the same size as a LCD screen [10]. A schematic diagram in Fig. 1.3 shows the basic components of typical FEDs. Field emission display is a low voltage display with a triode structure consisting of anode, cathode, and gate electrodes.

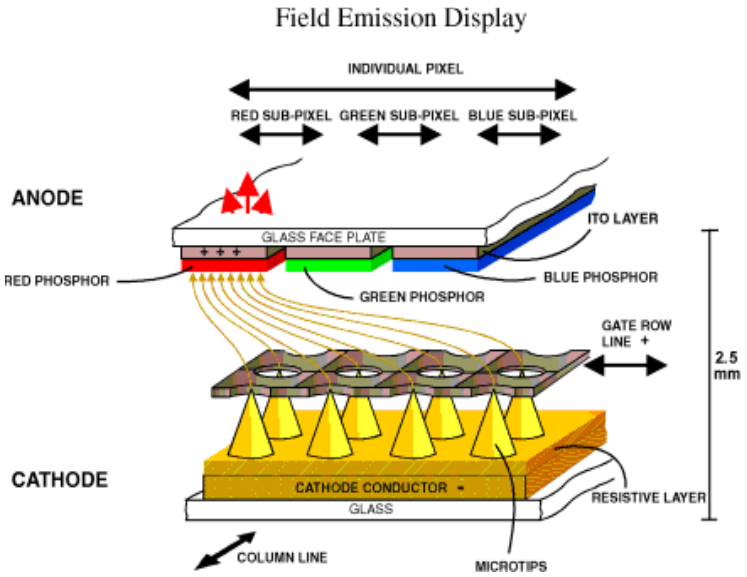


**Fig. 1.3** Schematic diagram of a FED display [11].

It utilizes substantially the same physical principle as the CRT, unlike CRT, FED relies on electric field or voltage induced, rather than temperature induced emission to excite the phosphor by electron bombardment. To produce these emissions, FED has generally used a multiplicity of x-y addressable cold cathode emitters. The cathode electrode is formed on a substrate on which the electron emission source is placed and an insulating layer and the gate electrode are formed on the cathode electrode. Images are formed using cold cathode electrons as an electron emission source.

A strong electric field is formed between a field emitter and the gate electrodes disposed on a cathode at constant intervals, so that electrons are emitted on the emitter and impact on phosphor on an anode, thereby emitting light. Its advantages are high brightness and self luminescence like CRTs and light weight and thin profile like LCDs. When they operate nearly all of the emitted electron energy is dissipated on phosphor bombardment and the electron of emitted unfiltered visible light [12].

### 1.3.3 Other Applications of phosphors

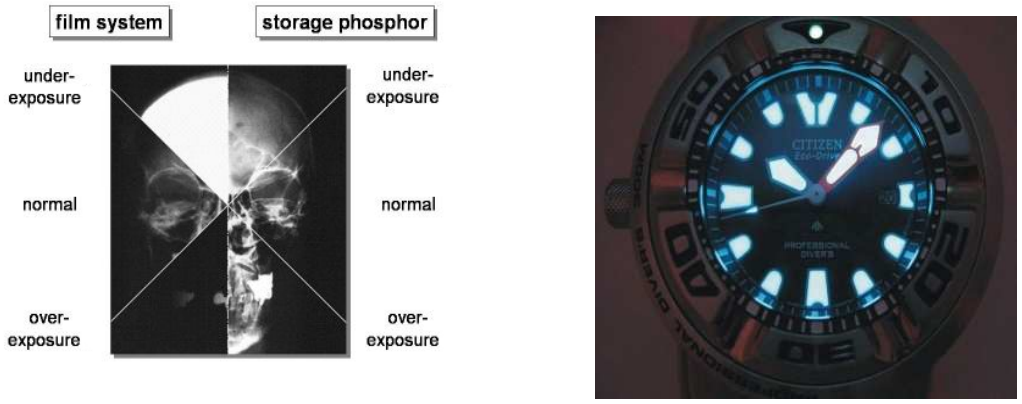


(a) (b)

**Fig. 1.4 (a)** X-ray storage phosphor and **(b)** Luminescent paint pigment applied on a driver's watch [13, 14].

Fig. 1.4 shows other examples of phosphor applications. In Fig. 1.4 (a) phosphors can be used as x-ray storage phosphor in computed radiography to generate digital radiographic images [15] and in (b) as luminescent watches to be used at night especially by drivers.

## 1.4 Light emission by phosphors

When a phosphor is exposed to primary radiation (excitation energy), either the host lattice absorbs excitation energy and transfer it to an activator resulting in light emission or the activator absorbs the excitation energy and transfers it to a neighbouring activator (usually identical to the latter) also resulting in light emission. When the activator absorbs the excitation energy, an electron from its ground state is raised to an excited state. The excited electron returns to the ground state by emitting light in the form of photons.

This process of light emission is called luminescence. Thus luminescence can be defined as emission of light occurring when excited electrons emit photons when returning to ground state. An unwanted process, called non-radiative process, where the excitation energy is dissipated as phonons when the electron returns to the ground is also possible.

### 1.4.1 Phosphorescence and fluorescence processes

Phenomenon of luminescence can be divided into two kinds, namely phosphorescence and fluorescence. Phosphorescence is a sustained glowing after exposure to energized particles such as electrons or ultraviolet photons whereas in fluorescence light emission from a substance stops immediately after excitation radiation. Basically, the word phosphorescence was derived from the word phosphor and fluorescence was introduced to distinguish the emission from phosphorescence [1].

### 1.4.2 Mechanism of Luminescence

The configuration coordinate model describes the electronic transitions of absorption and emission, in particular the effect of lattice vibrations, of a localized center. The diagram ((Fig. 1.5 (a)) depicts the energy of the ground state and first excited state of the impurity center as a function of normalized lattice position. The equilibrium atomic (lattice) configuration is determined by electronic distribution of the system which is due to the lattice distortion around the impurity [16].

In Fig. 1.5 (a) optical absorption and emission processes are indicated by vertical broken arrows. At zero temperature (T = 0K), an electron is raised from the ground state position A to the excited position B by the absorption of energy (transition A → B). Electronic transition occurs in a short time as compared to the time needed for an ion to move to a noticeable degree, thus this vertical transition follows Franck Condon principle. Consequently, the excited electron can further relax to equilibrium (new minimum energy) position C, before it emits luminescence. The energy difference between B and C is given off as lattice vibrations (phonon emission) which are accommodated by the atomic displacement from A to C. The center can further relax to the ground state (transition C → D) by photon emission.

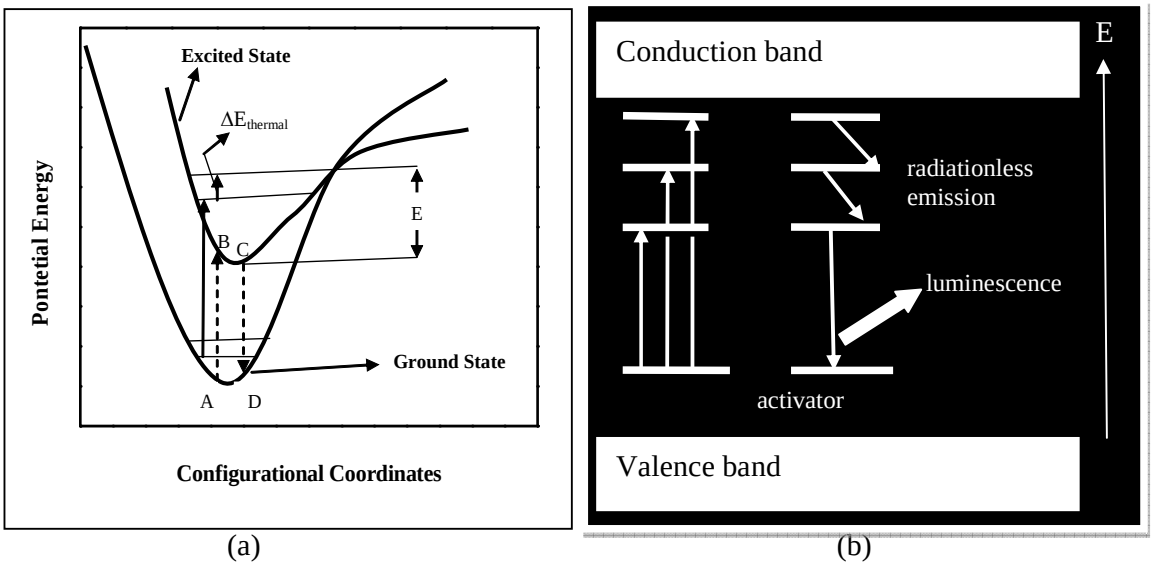


**Fig. 1.5 (a)** A schematic illustration of a configurational coordinate model [16] **(b)** Schematic of Energy band diagram showing transformation of excitation energy through radiative and non-radiative routes.

Equilibrium is again attained by phonon emission through atomic displacement from D → A. Because of phonon emission, the energy of the photon emitted will be smaller (Stokes shift) than that of the absorbed photon. In the case of overlapping of excited and ground state, the relation is non-radiative by multi-phonon emission (position E) due to thermal energy. The degree of overlapping of the two curves and the strength of local phonon coupling play important role for such non-radiative emission and the impurity is referred to as a killer center if no-radiation predominates [16]. Fig. 1.5 (b) is showing the related absorption and emission band in this non-radiative process.

### 1.4.3 Main processes of Luminescence

In general the luminescent process can be divided into three steps, namely excitation energy absorption, energy transfer, and light emission. The excitation energy can be absorbed by an activator or the host lattice and then transferred to the luminescent centre. This implies that energy transfer of the absorbed energy to the luminescent center take place before emission can occur.

The migration of energy absorbed by the lattice can take place through one of the following processes:

- Migration of electric charge (electrons, holes),
- Migration of excitons,
- Resonance between atoms with sufficient overlap integrals and,
- Re-absorption of photons emitted by another activator ion or sensitizer [17].

Based upon different types of transitions involved, the different processes of luminescence are shown in Fig. 1.6. Luminescence is divided into two major types, namely extrinsic and intrinsic luminescence. In the former there are two kinds, localized and unlocalized type of emission. The latter is divided into three kinds, band to band luminescence, exciton luminescence and cross luminescence.

#### 1.4.3.1 Extrinsic Luminescence

Extrinsic luminescence is caused by incorporated impurities (metallic or defects). Most observable phosphors that are of use in practical applications belong to this category of luminescence. In ionic crystals and semiconductors extrinsic luminescence is classified into two types known as unlocalized and localized type of emission.

Unlocalized luminescence depends on whether the excited electrons and holes of the host lattice participate in luminescence process and localized luminescence on whether the luminescence excitation and emission process are confined to localized centers [8].

#### 1.4.3.2 Intrinsic Luminescence

##### 1.4.3.2.1 Band to Band Luminescence

This type of luminescence is observed in a very pure crystal. Electrons in the conduction band recombine with a hole in the valence band, thus this process lead to emission of light [8].

#### 1.4.3.2.2 Exciton Luminescence

Exciton is a complex particle of an excited electron and a hole interacting with one another. Usually it moves in a crystal at the same time transferring energy and ultimately emission due the recombination of the electron and the hole [8].

#### 1.4.3.2.3 Cross Luminescence

Electrons in the valence band recombine with a hole in the outermost core band. Cross luminescence is only observed when the energy difference between the bands (outermost core band and the top valence band) is smaller than the band-gap energy [8].

Shown in Fig. 1.6 is a flow chart illustrating the different processes of luminescence and the nature of transitions involved.

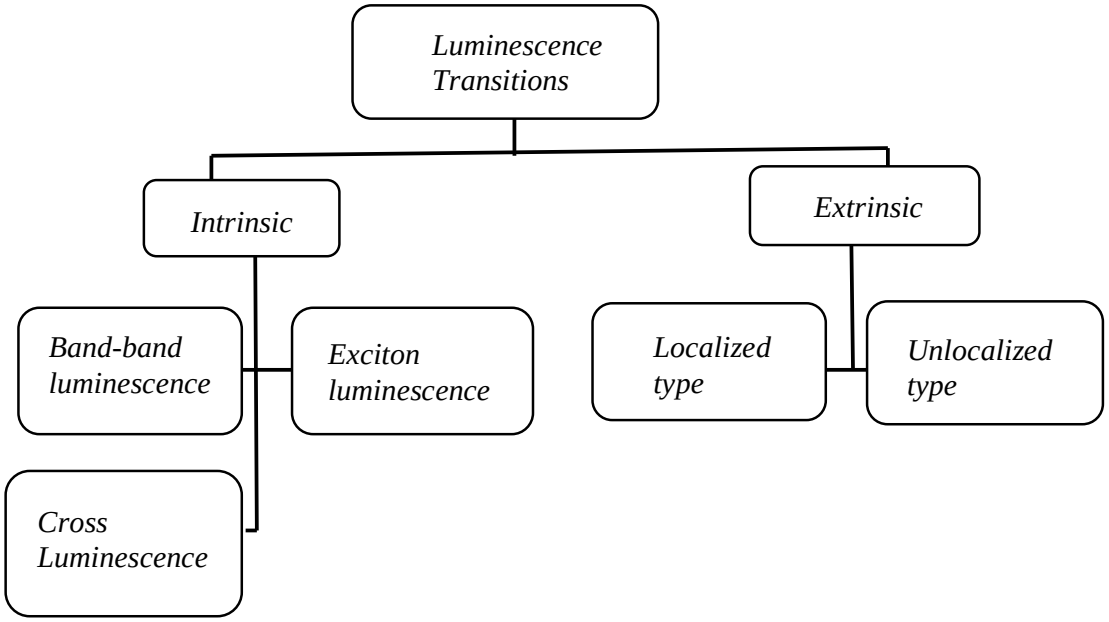


**Fig. 1.6** Different processes in luminescence based on nature of transitions involved.

The occurrence of energy transfer within a luminescent material has far reaching consequences for its properties as a phosphor. The absorbed energy can migrate to the crystal surface or to the lattice defects, where it is lost by radiationless deactivation. As a consequence the quantum efficiency of the phosphor will decline [17, 18].

There are a vast number of applications of these rare-earth activated materials and much of today's cutting edge optical technology and emerging innovations are enabled by their unique properties [19].

## 1.5 Rare earth Luminescence

Rare-earth ions have a multitude of technological applications as optically active impurities in insulator semiconductors. Knowledge of the energies of the host crystal's electronic band states relative to the $4f^N$ or $4f^{N-1}\ 5d^1$ states responsible for the ion's optical transition is important for understanding the properties and performance of each material since energy and electron transfer between these states influences the material efficiency and stability. Little is known about the relationship between these states, but there is growing motivation to explore these properties for developing ultraviolet laser materials, phosphors for application in field emission and plasma displays. Continued advances in optical technologies require knowledge of the systematic trends and behavior of rare-earth energies relative to crystal band states so that the properties of current materials may be fully understood and new materials may be logically developed [20].

Specific applications may employ the rare earth atomic-like $4f^N$ to $4f^{N-1}$ optical transition when, long lifetimes, sharp absorption lines, and excellent coherence properties are required, while others may employ the $4f^N$ to $4f^{N-1}\ 5d^1$ transitions when, large oscillator strengths, broad absorption bands, and shorter lifetimes are desirable [19]. The 4f electronic energy levels are characteristics of each ion. These are not affected much by the environment (ligand ions in the crystal) because of their shielded character from the outer $5s^2\ 5p^6$ electrons [1].

### 1.5.1 $Ce^{3+}$ (Cerium) Luminescence

Free trivalent $Ce^{3+}$- ion with the $[Xe]4f^1$ electron configuration has two $4f^1$ (ground state) levels, namely, the $^2F_{5/2}$ and $^2F_{7/2}$ separated by 2000 $cm^{-1}$ due to spin orbit coupling [21]. The spin-orbit interaction splits the 14-fold degenerates level with the orbital angular momentum L = 3 and the spin S = ½ into two levels with J = L+S = 7/2 and J = L – S = 5/2, where J is the total angular momentum. The six-fold degenerates level with J = 5/2 lies lower than the J = 7/2 by about 0.3eV [22]. The $5d^1$ configuration (excited state) is split into 2 or 5 components by the crystal field.

Emission occurs from the lowest crystal component of the $5d^1$ configuration to the two levels of the ground state. This gives the $Ce^{3+}$- ion emission its typical double band shape [21].

## 1.6 Ternary Sulfide phosphors and CL properties

The long history of investigation, the widest possible application, a variety of models, and perpetual studies – these are the traits of phosphors based on alkaline earth sulfides. They have attracted a lot of attention for a wide range of photoluminescence, cathodoluminescence and electroluminescent applications. Binary and ternary sulfide types of host are two commonly studied luminescent materials. Out of these, the ternary sulfide of type $M^{IIA}M^{III}A_2(S)_4$, where $M^{IIA}$ and $M^{III}$ represent group IIA and group III members of the periodic table, offer better CL efficiencies and structural properties for applications in information displays unlike the simple binary sulfides.

For cathode ray excitation at high voltage (>10kV), generally, zinc sulfide and alkaline earth binary sulfides (CaS, SrS) based phosphors show better luminescent properties than oxides, because of small bandgaps and rather low longitudinal optical (LO) phonon energy [23]. However, for FED applications, these phosphors show saturation because of low voltage and high current densities and lead to electron-induced decompositions [24, 25]. Moreover, the evolved gases like $SO_2$ contaminate the emitter tips and hence, reduce the lifetime of the emitters. It has been reported that $SrGa_2S_4$ based phosphor is a promising candidate for FEDs because of its good chromaticity, stability, and high luminance at low voltage and high current density excitation. Hence Ce- and Eu- doped $SrGa_2S_4$ have been widely studied as possible blue and green phosphor materials [26, 27, 28, 29].

Upon doping with $Ce^{3+}$- or $Eu^{2+}$- ion, the luminescence can be varied over the entire visible region by appropriately choosing the composition of the sulfide host. The photoluminescence (PL) spectra, cathodoluminescence (CL) efficiencies and structural properties of $Eu^{2+}$- and $Ce^{3+}$- doped $SrGa_2S_4$ powders were reported by Peters and Baglio and Donohue and Hanlon [30, 31]. The $Eu^{2+}$- doped $SrGa_2S_4$ compound is an efficient green phosphor, with excellent colour coordinates (x = 0.26, y = 0.69), high lumen equivalent (560l $m.W^{-1}$) and fast luminescence decay (480 ns) [32]. It has been claimed as a promising alternative to the standard green emitter in cathode ray tube (CRT) systems, the P22 ZnS:Cu phosphor.

The low saturation effects of $SrGa_2S_4:Eu^{2+}$ as well as $SrGa_2S_4:Ce^{3+}$, make it very advantageous for applications were high beam currents are required to achieve the wanted brightness levels in field emission display (FED) and (CRT) projection tube [33, 34]. The fast decay of the activator and the low concentration quenching allowing high activator doping reduce the ground state depletion and explain the high saturation resistance of these phosphors become increasingly inefficient below 5 kV because of non-radiative de-excitation losses by surface or near-surface defects in the surface dead layer.

Recently, alkaline earth thiogallates ($Ce^{3+}$- and $Eu^{2+}$- activated $SrGa_2S_4$) were investigated for application as a thin film phosphor in electroluminescent displays. Besides causing saturation effects, the high currents required in applications such as FEDs or CRT projection tube lead also to surface degradation, thermal quenching, heat damage and out gassing of the phosphors. These limiting problems can be reduced by the use of thin films. However, thin film luminous efficiencies are lower than those of powders due to light piping effect and lower photon–solid interaction volume [35, 36].

An extensive research on the luminescent materials applied in displays has been conducted for more than 50 years now. Compounds with almost ideal properties (very high energy efficiencies for CRT phosphors) have been prepared and investigated. Nevertheless, materials research is still going on, although it is focusing more on optimization of topology of phosphor layers, morphology of phosphor particles and degradation effects etc. However, new concepts are still needed to obtain materials surpassing the phosphors currently in use [13].

## 1.7 Origin of the Problem

In a search for a new phosphor that can be used in low voltage field emission displays (FEDs), cathodoluminescence intensity degradation of cerium doped strontium thiogallate ($SrGa_2S_4:Ce^{3+}$) was investigated. In addition to a high vacuum pressure, FEDs are designed to give a good performance at low accelerating voltages ($\leq$ 1kV) and higher current densities, in order to maintain adequate screen brightness. High current density often causes degradation of the phosphor screen due to charge loading at the surface. Therefore, FEDs phosphor should exhibit a good stability under electron bombardment [37].

In the present study, the CL intensity degradation of $SrGa_2S_4:Ce^{3+}$ was investigated at different accelerating voltages and oxygen pressures. In both powder and thin film forms, the effects of the prolonged electron beam exposure on the CL intensity degradation of $SrGa_2S_4:Ce^{3+}$ were investigated. The synergies between the CL intensity degradation and the surface chemical reactions were also investigated. Previous studies on the properties of $SrGa_2S_4:Ce^{3+}$ phosphor were on colour saturation and the brightness hence in this study the focus is mainly on the chemical stability of the phosphor.

## 1.8 Study objectives

- Investigation of the CL intensity degradation of commercial $SrGa_2S_4:Ce^{3+}$ phosphor in powder and thin film forms.
- Preparation of $SrGa_2S_4:Ce^{3+}$ phosphor thin films by pulsed reactive cross laser ablation (PRCLA) technique.
- Structural, morphological and chemical composition investigation of $SrGa_2S_4:Ce^{3+}$ powders and thin films.

## 1.9 Thesis Layout and experimental approach

The rest of the chapters in this dissertation are in the following order:

- Chapter 2 deals with the theory of the research techniques used in this study. A brief description of working principle for each technique is discussed.
- In Chapter 3, results on luminescent properties (CL and PL), structural properties (XRD) and morphology (SEM) of commercially available $SrGa_2S_4:Ce^{3+}$ are discussed.
- Chapter 4 discusses the results on the CL degradation and chemical changes that took place on the surface chemistry of the powder phosphor during prolonged electron irradiation.
- Chapter 5 gives a summary of the PRCLA deposition method used to deposit thin films of $SrGa_2S_4:Ce^{3+}$ phosphor. The results on luminescent properties (PL and CL), structural properties (XRD), and morphology (SEM) of the films prepared are also discussed.

- Chapter 6 discusses the results on the CL degradation and changes that took place on the surface chemistry of the thin films during electron irradiation.
- Chapter 7 gives the summary of the thesis, conclusion and discussion on powder and thin films and suggestions for possible future studies on this phosphor.

The objectives of this study listed above will be achieved using the following techniques:

- PL for light emission by photon excitation.
- CL for light emission by electron excitation.
- XRD for structure and particle size analyses.
- SEM for morphology and size.
- AFM for surface topography.
- EDS for chemical composition of elements.
- AES for monitoring surface composition during degradation.
- XPS for surface chemical state.

## References

[1] W M Yen, S Shionoya and H Yamamoto, *Phosphor Handbook*, 2nd edition, Tailor and Francis Group, LLC (2007).

[2] L Ozawa, *Cathodoluminescence and Photoluminescence: Theories and Practical Applications,* CRC Press, Taylor and Francis Group, LLC (2007).

[3] http://www.ustr.net/electronics/fluorescent.shtml.

[4] http://www.ablamp.wordpress.com/2007/60/12/save-energy-money-and-the-environment-with-compact-fluorescent-light-bulbs/energy-saving-compact-fluorescent-light-bulb/.

[5] http://inventors.about.com/od/cstartinventions/a/CathodeRayTube.htm/.

[6] http://jegsworks.com/Lessons/lesson5/lesson5-4htm.

[7] http://searchcio-midmarket.techtarget.com/sDefinition/0,,sid183_gci213839,00.html.

[8] D R Vij, *Luminescence of Solids,* Plenum Press, New York, (1998)

[9] M M Biggs, MSc. Dissertation, University of the Free State, South Africa (2009).

[10] A Dhir, *The Digital Consumer Technology Handbook*, Xilinx, Inc. (2004)

[11] http://grops.csail.mit.edu/graphics/classes/6.837/F01/Lecture01/Slide20.html.

[12] http://www.electronics-manufacturers.com/products/video-equipment/field-emission-display/

[13] http://fb6www.unipaderborn.de/ag/ag-schweizer/research/x-ray_storage_phosphors.html.

[14] F Flinch, http://en.wikipedia.org/wiki/ (26 April 2008).

[15] http://www.alara.com/about/sp.html.

[16] D R Vij, N Singh, *Luminescent and Related Properties of II-VI Semiconductors* (1998).

[17] D V Rosse, *Focus on Material Science Research*, Nova Science Publishers (2007).

[18] T Jüstel, H. Nikol and C Ronda, *Angew. Chem. Int. Ed.*, **37**, 3084-3103 (1998).

[19] C W Thiel, Y. Sun and R. L. Cone, *Journal of Modern Optics*, **49**, 2399 (2002).

[20] C W Thiel, H Cruguel, H Wu, Y Sun, G Lapeyre, R W Equally and R. M. Macfarlane, *Optics and Photonics News*, **12** (12), 64 (2001).

[21] G Blasse and B C Grabmaier, *Luminescent Materials*, Springer-Verlag (1994).

[22] Y Kuramoto and Y Kitaoka, *Dynamic of Heavy Electrons*, Oxford University Press Inc, New York (2000).

[23] T E Peter and J A Baglio, *J. Electrochem. Soc.*, ***119****, 230 (1972)*, D J Robbins, *J. Electrochem. Soc.*, **127**, 2694 (1980].

[24] S Itoh, T Watanabe, K Ohtsu, M Uyokoyama, and M Taniguchi, *J. Electrochem. Soc.*, **136**, 1819 (1989).

[25] P H Holloway, T A Trottier, J Sebastian, S Jones, X M Zhang, J S Bang, B Abrams, and W J Kim, *Extended Abstract of the 3rd International Conference on Science and Technology of Display Phosphors*, Hungtington Beach, CA, p.7, (1997).

[26] F E Zhang, S Yang, C Stoffers, J Penczek, P N Yocom, D Zaremba, B K Wagner and C J Summers, *Appl. Phy. Lett.*, **72**, 2226 (1998).

[27] O N Dyazorski, T Mikami, K Ohmi, S Tanaka, and H Kobayashi, *J. Electrochem. Soc.*, **146**, 1215 (1999).

[28] P D Rack, T A O'Brien, M C Zerner, and P H Holloway, *J. Appl. Phys.,* **86**, 2377 (1999.

[29] P Benlloul, C Barthou, J Benoit, L Eichenawer, and A Zeirert, *Appl. Phys. Lett.*, **63**, 1954 (1993).

[30] T E Peters and J A Baglio, *J. Electrochem. Soc.* 119, 230 (1972).

[31] P C Donohue and J E Hanlon, *J. Electrochem. Soc.* 121, 137 (1974).

[32] C Chartier, C Barthou, P Benalloul and J Frigerio, *Journal of Luminescence,* **111**, 147-158 (2005)

[33] I Ronot-Lumousin, A Garcia, C Fouassier, C Barthou, P Benalloul and J Benoit, *J. Electrochem. Soc.* **144,** 687 (1997).

[34] S Yang, C Stoffers, F Zhang, B K Wagner, J Penczek, S M Jacobsen, C J Summers and P N Yocom, *Appl. Phys. Letter.* **72**, 158 (1998)

[35] C Chartier, P Benalloul, C Barthou, J-M Frigerio, G O Mueller, R Mueller-Mach and T Trottier, *J. Phys. D: Appl. Phys.* **35**, 363-368 (2002).

[36] S Okamoto, K Tanaka, and Y Inoue, *Appl. Phys. Lett.*, **Vol. 76**, No. 8, 21 Feb(2000).

[37] A Lakshmanan, *Luminescence and Display Phosphor,* Nova Science Publishers (2008).

# CHAPTER 2

# THEORY OF RESEARCH TECHNIQUES

## (Principles of Operation)

### Introduction

*This chapter gives an introduction to the theory of research techniques used in this study. These include pulsed laser deposition (PLD) technique, pulse reactive cross laser ablation technique (PRCLA), scanning electron microscopy (SEM), atomic force microscopy (AFM), Luminescence (photoluminescence and cathodoluminescence) spectroscopy, UV-Vis absorption spectroscopy, energy dispersive x-ray spectroscopy (EDX), Auger electron spectroscopy (AES), x-ray photoelectron spectroscopy (XPS) and X-ray diffraction (XRD).*

## 2. 1 Pulsed Laser Deposition (PLD) Technique

Pulsed laser deposition is a physical vapour deposition process, carried out in a vacuum system that shares some process characteristics common with molecular beam epitaxy (MBE) and some with sputter deposition [1]. Shown in Fig. 2.1 are PLD set-up and the stages involved in the deposition process, starting from when the high energy laser pulse impinges on ablation target. After the laser is absorbed by the target, a highly forward directed plasma plume traverses away from the target and ablated atoms are collected on the substrate, thus, leading to a thin film growth.

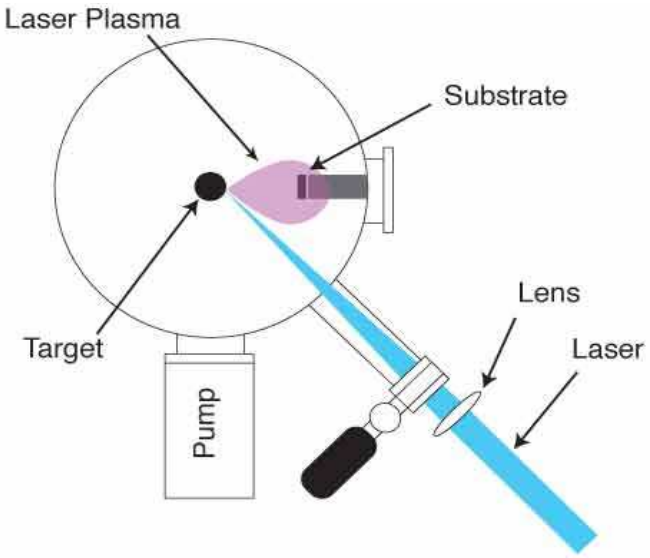


**Fig. 2.1** Schematic diagram of a typical laser deposition set-up [2].

In the PLD technique, a high power laser is used as an external energy source and is focused on a target (a pelletized phosphor) mounted on a rotating sample holder. Upon contact with the higher energy laser, the target will be ablated in the form of a plasma plume which will subsequently be deposited on the heated substrate. Background gases like $O_2$, Ar and $N_2$ can be introduced in the chamber to promote gas phase reactions, surface reaction, or to maintain the film stoichiometry [3].

## 2. 2 Pulsed Reactive Crossed-Beam Laser Ablation (PRCLA) Technique

Pulsed Reactive Crossed-Beam Laser Ablation (PRCLA) is a simple but powerful adaptation of pulsed laser deposition through which a synchronized gas pulse crosses the ablation plume

close to its origin, as shown in Fig. 2.2, increasing the gas phase interaction and the probability of reactive scattering, and also allowing the resulting species to propagate freely away from the localized scattering region [2].

In reactive PLD, a gas is introduced into the film growth chamber in order that the chemistry of the growing film compensate for deficiencies of ablated materials. For example Gupta and Hussey used $O_2$ to compensate for oxygen deficiency in their experiment [5]. The use of a synchronized pulsed gas source enables one to limit the delivery of gas to the time period when transfer and deposition of ablated material occurs [4].

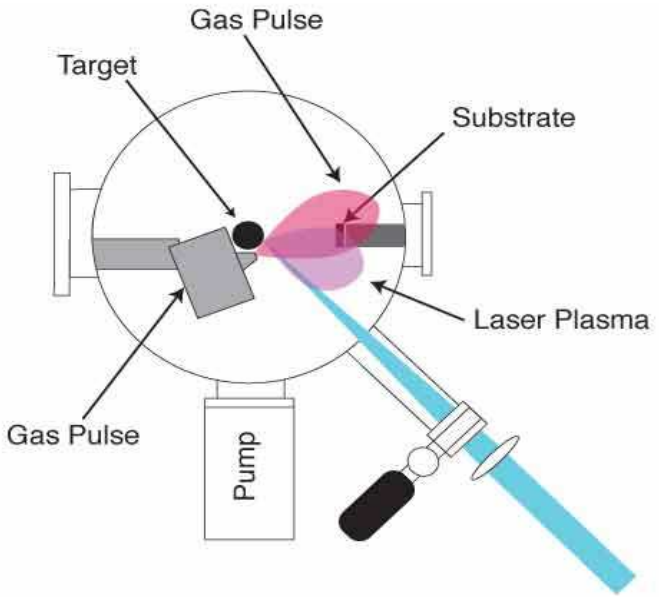


**Fig. 2.2** Schematic of Pulsed reactive crossed-beam laser ablation set up [2]

Keeping the distance between the pulsed valve gas nozzle and the ablation laser focus point to less than approximately 10 mm, couples some of the internal and kinetic energy of the ablation plume species to the gas pulse. That is, as the plasma expands and propagates through the gas pulse, which is a transient high pressure region, it transfers some of its energy to the gas particles via collision [6]. Thus, these initial collisions and the afterwards free expansion provide and maintain the reactivity for enhanced film growth [4].

A fundamental advantage of using a gas pulse is that after its interaction with the ablation plasma, it rapidly expands into a vacuum, the distance between the gas particles increases, and collisions become rare. Therefore, species excited by the collisions that occur before the pulse has expanded, maintain their reactivity as they rapidly enter collision-less conditions

[7]. The potential advantages of reactive PLD over conventional PLD are well illustrated in compound semiconductor growth. For example, films of the III–V optical semiconductors GaN, AlN, and InN have been grown by the use of metallic targets (Ga, Al, or In) in a $N_2$ or $NH_3$ background [4].

It was observed that the purity of electronics grade Ga metal, ammonia, and $N_2$ is sufficient for high quality film growth. Attempts were made to grow GaN by reactive PLD using a liquid Ga ablation target and were successful with the use of a static $NH_3$ as the ambient, but only became possible with $N_2$ at pressures of the order of $10^2$ Pa. Later Phillip Willmot et al [7], in their laboratories started growing GaN and $Al_xGa_{1-x}N$ using PRCLA at low average background gas pressures. During their investigation, the following long standing problems were resolved namely, (1) it was possible to grow GaN and $Al_xGa_{1-x}N$ at low temperatures without hydrogen-containing precursors, (2) and by using high purity material, the problems associated with sintered ablation targets could be circumvented.

Modern excimer lasers commonly used for the process of ablation of materials are ArF (193nm), KrF (284nm), XeCl (308nm) and $F_2$ (157nm). A XeCl 309nm laser wavelength PLD system at Stellenbosch University (Physics department) was used in the current study (Fig. 2.3) to deposit thin films.

**Fig. 2.3** The Pulsed Laser Deposition (PLD) machine at Stellenbosch University, Physics department.

## 2. 3 Photoluminescence (PL) Spectroscopy

In a PL system the sample is excited with a monochromatized lamp or a higher laser beam, which is followed by the excitation during electron transition to higher energy levels and emission of photons during transition to the ground state. Care should be taken to ensure that the wavelength selected does not cause sample decomposition. Emitted light is directed by focusing lenses and analyzed by means of a monochromator, which is followed by a photo-sensor connected to a computer. From this process, two kinds of spectra, namely (1) emission and (2) excitation spectra can be recorded [8, 9].

- When emission spectrum is taken, the excitation wavelength is fixed and the emitted light intensity is measured at different wavelengths positions by scanning the emission monochromator. For example, fixing the excitation energy at $hv_1$, consists of a single band that peaks (emission) at the same photon energy.
- When an excitation spectrum is taken, the emission monochromator is fixed at any emission wavelength value while the excitation wavelength is scanned in a certain spectral range. For example, setting the emission monochromator at fixed energy $h(v_2 - v_1)$, a single band is observed at $hv_2$ (emission) , that is, after the second state of the energy levels is populated [8].

Shown in Fig. 2.4 (a) is a typical experimental arrangement to measure photoluminescence spectra.

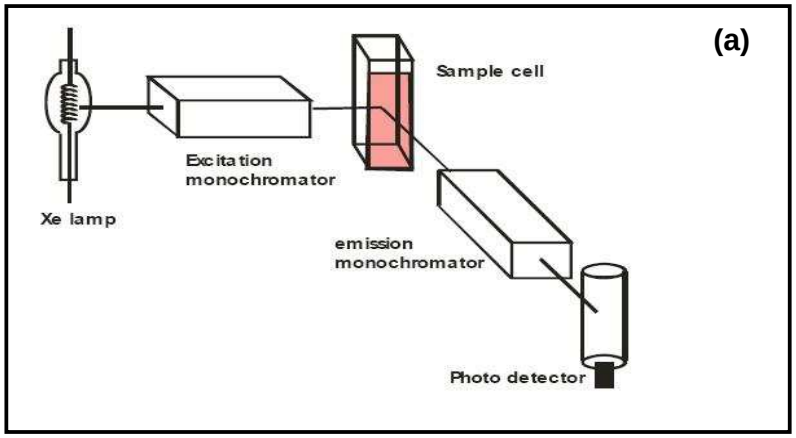


**Fig. 2.4 (a)** A schematic diagram showing the main elements for measuring photoluminescence spectra [10].

In this study, the photoluminescence (PL) (excitation and emission) spectra were measured using Varian Cary Eclipse fluorescence spectrophotometer, shown in Fig. 2.4 (b), using a monochromatized Xenon lamp (60-75W) as the excitation source whose wavelengths can be varied on the whole UV region.

(b)

**Fig. 2.4 (b)** The Cary Eclipse Fluorescence Spectrophotometer at the University of the Free State, Physics department.

## 2. 4 UV-Visible Spectrophotometery

Absorption spectra are measured using UV-Vis spectrophotometer. The main elements of the simplest spectrophotometer of a single beam configuration are shown in the schematic diagram in Fig. 2.5 (a). Some spectrophotometers consist of a double beam configuration.

Fundamentally, the spectrophotometer (single beam) consists of the following elements: (1) a light source (usually a deuterium lamp for the UV spectral range and a tungsten lamp for the VIS and IR spectral ranges). Normally they are focused on the entrance to (2) a monochromator, which is used to select a single frequency wavelength from all those provided by the lamp source and scan over a desired frequency range, (3) a sample holder, followed by (4) a light detector (usually a photomultiplier for the UV-VIS range and a SPb cell for the IR range) to measure the intensity of each monochromatic beam after crossing the sample. Lastly, a computer registers the absorption spectrum [8].

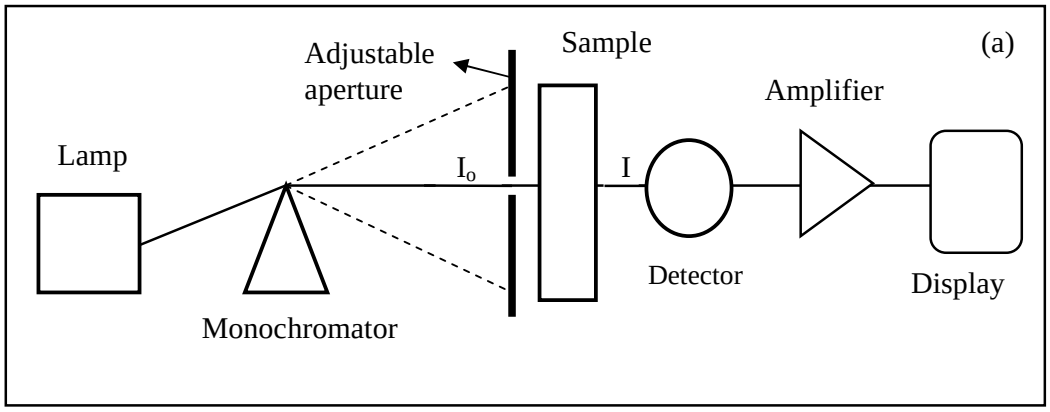


**Fig. 2.5 (a)** Schematic diagram of a single-beam spectrophotometer [11]

Optical spectrophotometers work in different modes to measure optical density (OD) absorbance (A) or transmittance (T). Absorption coefficient can be determined by measuring the optical density and the sample thickness (equation 1).

According to Lambert-Beer Law*:* $I = I_o e^{-\alpha x}$, which gives an exponential attenuation law of the light intensity I, relating the incoming light intensity $I_o$ (i.e. the incident intensity minus the reflection losses at the surface) to the thickness x. The absorption coefficient α, is given by:

$$\alpha = \frac{OD}{\mathrm{x}\log \mathrm{e}} = \frac{2.303(OD)}{\mathrm{x}} , \quad OD = \log\left(\frac{I_o}{I}\right) , \text{ where} \tag{2.1}$$

α is an absorption coefficient of the material, *OD* is the optical density, *I* the light intensity and x the sample thickness. Well known optical magnitudes such as the transmittance and absorbance are also measured using spectrophotometers. They can easily be related to optical density through the relation (equation 2.2).

$$T = 10^{-OD} , \quad T = \frac{I_o}{I} \qquad \text{and} \qquad A = 1 - 10^{-OD} , \quad A = 1 - \frac{I_o}{I} \tag{2.2}$$

Different numbers of problems are experienced with a single beam spectrophotometer when measuring, such as spectral variations and temporal variations in the illumination intensity. These variations are attributed to the combined effects of the lamp spectrum and the monochromator response and the lamp stability respectively.

Now, to reduce these effects, double-beam spectrophotometers are used. In the double-beam spectrophotometer (Fig. 2.5 (b)), the illuminating beam is split into two beams of equal intensity, which are directed toward a reference channel and a sample channel. Two similar detectors (D1 and D2) detect the outgoing intensities corresponding to $I_o$ and I respectively. Therefore, both the reference and sample beam are affected by the temporal intensity variations of the illuminating beam in the same manner. But, these effects are minimized in the resulting absorption spectrum. The two detectors also introduce errors because of the usual non-exact equal spectral responses. To eliminate the problem, fast rotating mirrors are introduced so that the intensity $I_o$ and I can be sent always to the same detector [8].

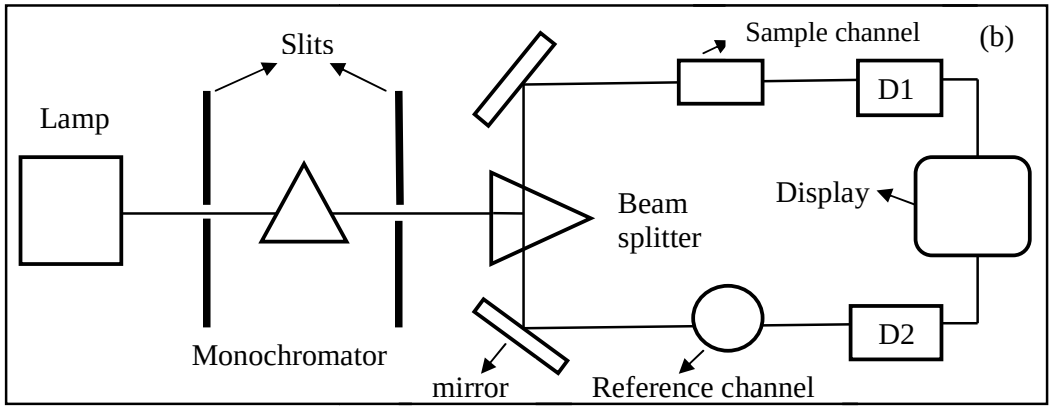


**Fig. 2.5 (b)** Schematic diagram of a double-beam spectrophotometer [12].

Shown below (Fig.2.5 (c)) is a UV-VIS spectrophotometer used to collect absorption and transmittance spectrums.

(c)

**Fig. 2.5 (c)** Perkin Elmer Lambda 950 UV-VIS Spectrometer at the University of the Free State, Physics department.

## 2. 5 X-Ray Diffraction (XRD)

X-ray diffraction is a rapid analytical technique primarily used for phase identification of a crystalline material and can provide information on unit cell dimensions. Now, is commonly used to study the crystal structure and atomic spacing. It is also most widely used for the identification of unknown crystalline materials (e.g. minerals and inorganic compounds) [13].

X-ray diffractometers consist of three basic elements: (1) an X-ray tube (cathode), (2) sample holder and (3) x-ray detector. In a tube, x-rays are generated by heating a filament and electrons are produced. Voltage is applied to accelerate the electrons towards a target and a target is bombarded with electrons. When electrons with sufficient energy dislodge inner shells electrons of the target material, characteristic X-ray spectra are produced consisting of the most common components, namely $K_\alpha$ and $K_\beta$. These X-rays are generated by a cathode ray tube, filtered to produce monochromatic radiation ($CuK_\alpha$ = 1.5418 Å), collimated to concentrate, and are directed towards the sample. Shown below (Fig. 2.6 (a)) is a simple schematic diagram of a path followed by x-ray from the tube to the detector.

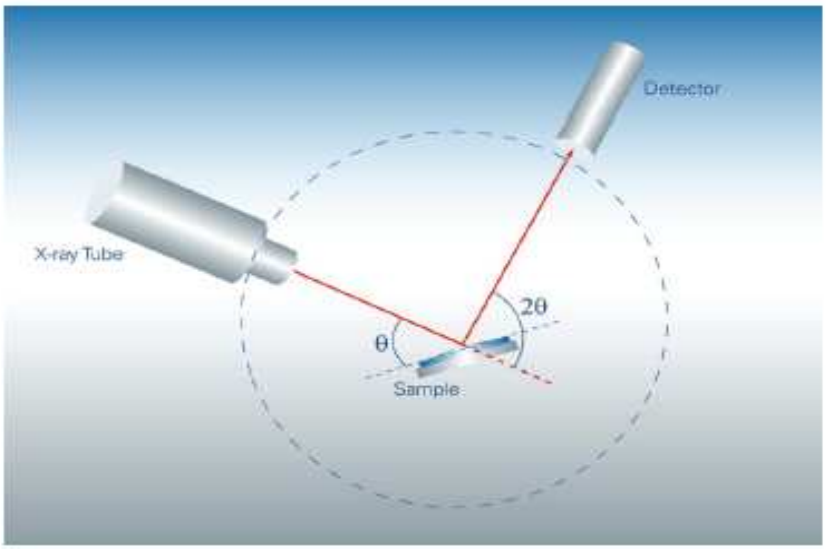


(a)

**Fig. 2.6 (a)** Schematic diagram of diffractometer system [14]

The interaction of the incident rays with the samples produces constructive interference, thus giving diffracted rays (detected, processed and counted) when conditions satisfy Bragg's Law

($n\lambda = 2d\ Sin\ \theta$). This law relates the wavelength of electromagnetic radiation to the diffraction angle and the lattice spacing in a crystalline sample.

Scanning the sample through a range of 2θ angles, all possible directions of the lattice should be attained due to the random orientation of the powdered material [13]. In this study D8 Advanced AXS GmbH X-ray diffractometer, shown in Fig. 2.6 (b), equipped with Cu $K_\alpha$ radiation was used.


(b)

**Fig. 2.6 (b)** D8 Advanced AXS GmbH X-ray diffractometer at the University of the Free State, Physics department.

## 2. 6 Scanning Electron Microscopy (SEM)

The scanning electron microscopy uses a focused beam of high-energy electrons to generate a variety of signals at the surface of solid specimen. Signals derived from the electron-sample interactions reveal information about the sample including external morphology (texture), chemical composition (when energy dispersive x-ray spectrometer (EDS) is coupled in the system), and crystalline structure and orientation of materials making up the sample [15]. In generally, the electron microscope consist of an electron source, an anode, magnetic lenses, apertures, specimen stage and image recording system all of which operate in a high vacuum.

The most common used electron source is the tungsten filament, but, they can be made of different types of material. Heating the filament, electrons are produced which are in turn attracted by the anode and accelerated down the column to interact with the specimen. Magnetic lenses are used to focus the electrons in the column and the apertures to filter out electrons in order to produce a monochromatic beam. Therefore, monochromatic beam interacts with the sample, this happens in many ways depending on the type of the electron microscope used. Detected interactions are converted into an image with the image recording system [16]. Schematic layout of a typical SEM is shown in Fig 2.7 (a).

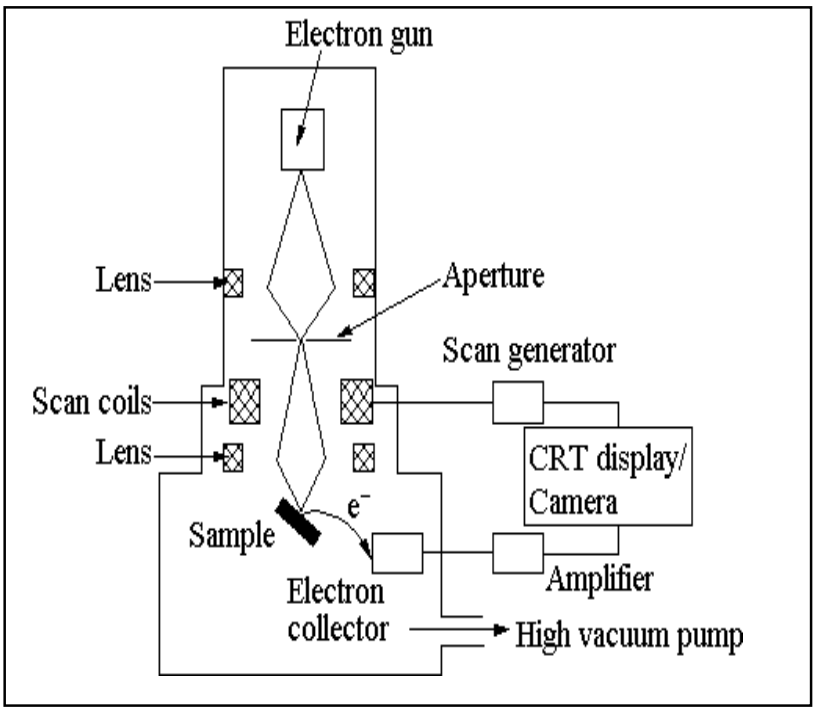


(a)

**Fig. 2.7 (a)** Schematic diagram of a Scanning Electron Microscopy [17]

In the SEM system, a set of scan coils moves the electron beam across the specimen in a two-dimensional grid fashion. When the electron beam scans across the specimens, different interactions take place which are decoded with various detectors situated in the chamber above the specimen. Some of the electrons from the surface material are knocked out of their orbital by the electron beam, and are called secondary electrons. These electrons are detected by the secondary electron detector.

Different interactions give images based on topography, elemental composition or density of the sample. A SEM can magnify up to about 100 000 times [16]. In this study two types of SEMs were used namely Shimadzu Superscan SSX-550 system and the PHI 700 auger Nanoprobe (Fig. 2.7 (b) and (c)).

(b)

(c)

**Fig. 2.7 (b)** Shimadzu Superscan SSX-550 SEM at the University of the Free State, Microbiology department. **(c)** PHI 700 Auger Nanoprobe SEM unit at the University of the Free State, Physics department.

## 2. 7 Atomic Force Microscopy (AFM)

Atomic Force Microscopy (AFM) is a form of scanning probe microscopy (SPM) where a small probe is scanned across the sample to obtain information about the sample's surface [18]. AFM provides a number of advantages over conventional microscopy techniques. It probe the sample and make measurements in three dimension x, y and z (normal to the sample surface), thus enabling the presentation of three dimensional images of a sample surface [19]. The remarkable feature of this technique is the ability to examine samples not only in an ultrahigh vacuum but also at ambient conditions or even in liquids [20]. Shown in Fig. 2.8 (a) is the schematic layout of the atomic force microscopy.

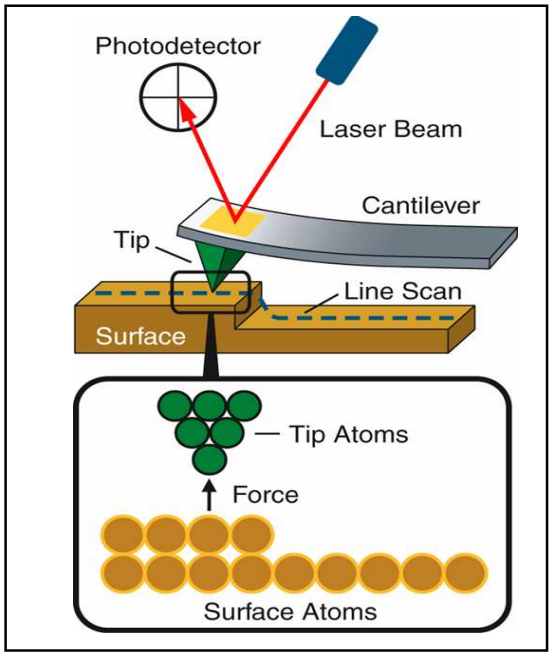


(a)

**Fig. 2.8 (a)** A simplified layout of Atomic Force Microscopy [21]

The AFM probe has a very sharp tip, often less than 100Å diameter, at the end of a small cantilever beam. The probe is attached to a piezoelectric scanner tube, which scans the probe across a selected area of the sample surface. Interatomic forces between the probe tip and the sample surface causes the cantilever to deflect as the sample's surface topography (or other properties) changes.

A laser light reflected from the back of the cantilever measures the deflection of the cantilever. This information is fed back to a computer, which generates a map of topography or other properties of interest. Areas as large as about 100 μm square to less than 100 nm square can be imaged [18]. AFM can work with the tip touching the sample (contact mode), or the tip can tap across the surface (tapping mode), or with the tip interaction with the sample minimized (non-contact mode) [22]. In the current study the AFM images were collected using Shimadzu SPM-9600 model.

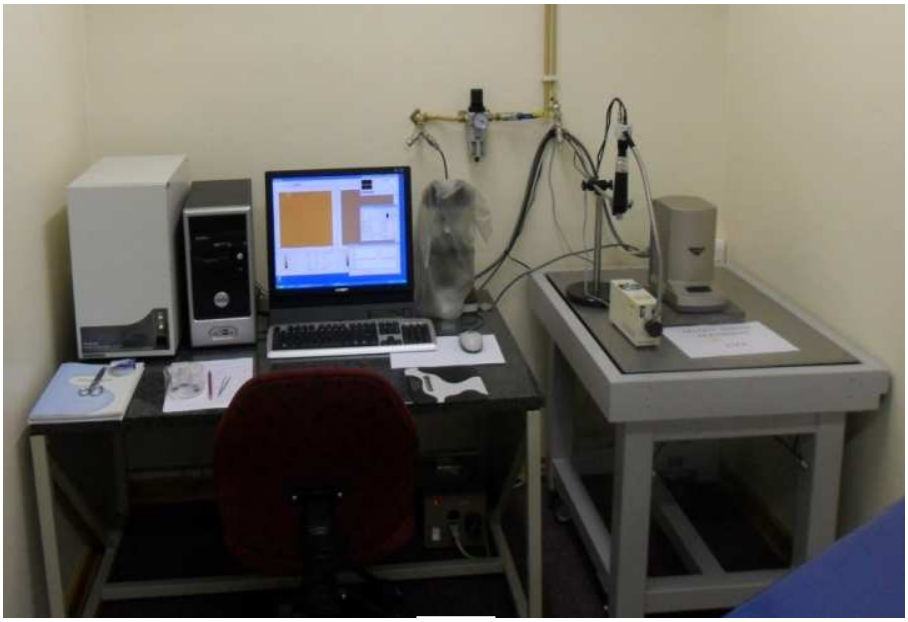

(b)

**Fig. 2.8 (b)** Atomic Force Microscopy at the University of the Free State, Physics department

## 2. 8 Auger Electron Spectroscopy (AES)

Auger Electron Spectroscopy (AES) is a technique that provides information about the chemical composition of the outermost material comprising a solid surface or interface. The principal advantages of AES over other surface analysis methods are excellent spatial resolution (< 1 μm), surface sensitivity (~20 Å), and detection of light elements [23].

In the AES, a primary electron beam is used to excite the sample surface. When electron is ejected from an inner shell of a sample atom the resultant vacancy can be filled by an electron from an outer shell.

To compensate for the energy change from this transition, an Auger electron or an X-ray is emitted. Basically this technique measures the energy of electrons emitted from a material. Therefore, the energy of the emitted Auger electron is characteristic of the element from which it was emitted. These auger electrons are detected and analysed and produce a spectrum of Auger electron energy versus the relative abundance of electrons. Auger electrons have relatively low kinetic energy, which limits their escape depth. Any Auger electrons emitted from an interaction below the surface will lose energy through additional scattering reactions along its path to the surface [18].

## 2. 9 Cathodoluminescence (CL) Spectroscopy

In this study, CL data was collected using the S2000 Ocean Optics spectrometer type with OOIBase32 computer software coupled with the PHI (model 549) Auger spectrometer. The CL data were collected using the optical fibre with one end connected to the spectrometer and the other end positioned inside the chamber close to the sample. Catholuminescence is an optical and electrical phenomenon where a beam of electrons generated by an electron gun impacts on a phosphor causing it to emit visible light [24]. Shown in Fig. 2.9 is the AES combined with the CL system used in this study.

**Fig. 2.9** PHI model 549 Auger Electron Spectroscopy (AES) unit coupled with the CL unit at the University of the Free State, Physics department.

## 2. 10 X-ray Photoelectron Spectroscopy (XPS)

X-ray photoelectron spectroscopy phenomenon is based on the photoelectric effect outlined by Eistein in 1905 where the concept of the photon was used to describe ejection of electrons from a surface when the photons impinge upon it. AlKα (1486.6eV) or MgKα (1253.6eV) are often the photon energies of choice [23]. Essentially, photoelectron spectroscopy utilizes photo-ionization and analysis of the kinetic energy distribution of the emitted photoelectrons to study the composition and electronic state of the surface region of a sample.

In XPS, the x-ray photon is absorbed by an atom in a molecule or solid, leading to ionization and the emission of a core (inner shell) electron. The kinetic energy distribution of the emitted photoelectrons (i.e. the number of emitted photoelectrons as a function of their kinetic energy) can be measured using any appropriate electron energy analyser and a photoelectron spectrum can thus be recorded.

The process of photo-ionization can be considered in several ways, one way is to look at the overall process as follows:

$$\mathbf{A} + h\nu \rightarrow \mathbf{A}^{+} + \mathbf{e}^{-} \qquad (2.1)$$

where A is the atom in a molecule or solid, $h\nu$ the photon energy, $A^{+}$ is the ionized atom and e- an electron.

Conservation of energy then requires that:

$$\mathbf{E(A)} + h\nu = \mathbf{E(A^{+})} + \mathbf{E(e^{-})} \qquad (2.2)$$

where E represent the energy. Since the electron's energy is present solely as kinetic energy (KE) equation 2 can be rearranged to give the following expression for the KE of the photoelectron:

$$\mathbf{KE} = h\nu - (\mathbf{E(A^{+})} - \mathbf{E(A)}) \qquad (2.3)$$

The final term in brackets, representing the difference in energy between the ionized and neutral atoms, is generally called the binding energy (BE) of the electron, this then leads to the following commonly quoted equation:

$$\mathbf{KE} = h\nu - \mathbf{BE} \tag{2.4}$$

For each element, there will be a characteristic binding energy associated with each core atomic orbital i.e. each element will give rise to a characteristic set of peaks in the photoelectron spectrum at kinetic energies determined by the photon energy and the respective binding energies. The presence of peaks at particular energies therefore indicates the presence of a specific element in the sample under study.

Furthermore, the intensity of the peaks is related to the concentration of the element within the sampled region. Thus, the technique provides a quantitative analysis of the surface composition and is sometimes known by the alternative acronym, ESCA (Electron Spectroscopy for Chemical Analysis) [24]. For collecting data in this study the PHI 5000 XPS Versaprobe (monochromatic AlKα lines) system was used (Fig. 2.10).

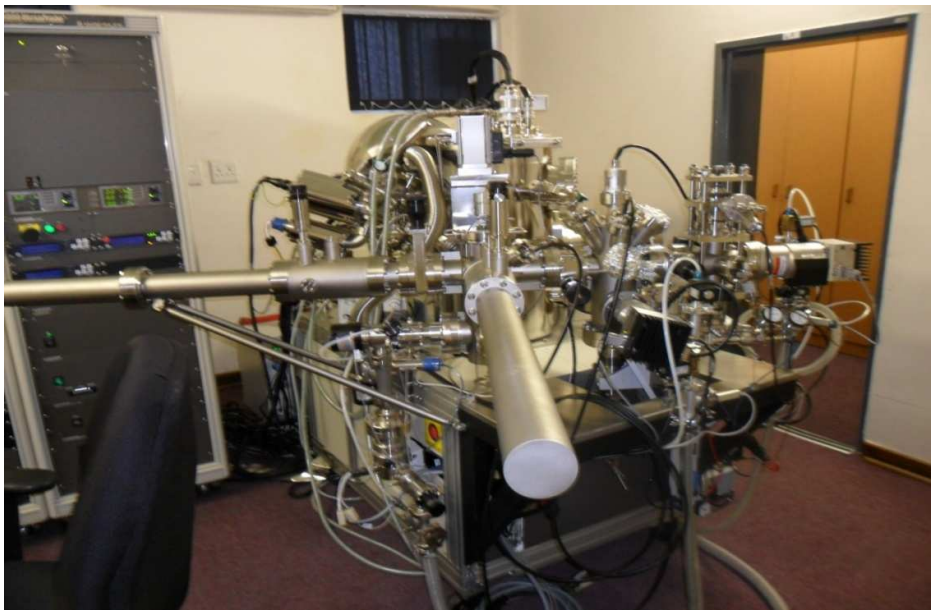

**Fig. 2.10** The PHI 5000 XPS Versaprobe (monochromatic AlKα lines) machine at the University of the Free State, Physics department.

## References

[1] R Eason, *Pulsed Laser Deposition of Thin Films*: Applications-Led Growth of Functional Materials, A John Wiley & Sons (2007).

[2] http://material.web.psi.ch/Research/Thin_Films/Methods/PLD.htm, Paul Scherrer Institute, Material Group, 5232 Villigen PSI, Schweiz.

[3] M M Urtasun, PhD Dissertation, Universität Zürich (2005).

[4] P R Willmot, *Appl. Phys. A **69** [Suppl]*, S437-S440 (1999).

[5] A Gupta and B W Hussey, *Appl. Phys. Lett.* **58,** 1211 (1991).

[6] S Angappane, N R Selvi and G U Kulkarni, *Bull. Mater. Sci.*, Vol 32, No. 3, pp 253-258, June (2009).

[7] http://www.pci.uzh.ch/pfister/ftp/Synthesis_preprint.pdf. P RWillmott, H Spillmann, J R Huber,

[8] J G Solé, L E Bausá and D Jacque, *An Introduction to the Optical spectroscopy of Inorganic Solids*, John Wiley & Sons, Ltd (2005).

[9] http://analyticalspectroscopy.net/ap2-8.htm

[10] http://www.sas.upenn.edu/~kimg/mcephome/chem507/fluorimeter.JPG.

[11] http://www.upload.wikimedia.org/wikipedia/commons/thumb/Spectrophotometer/

[12] http://www.boomer.org/c/p1/Ch02/Ch0207.html

[13] http://serc.carleton.edu/research_education/geochemsheets/techniques/XRD.html
B L Ditrow and C M Clarke

[14] D8 Advance User manual, DOC-M88-EXX153 V1-09.2009

[15] http://serc.carleton.edu/research_education/geochemsheets/techniques/SEM.html.
S Swapp.

[16] http://www.physchem.co.za/OB12-way/microscope.htm

[17] http://www.chm.bris.ac.uk/pt/diamond/stuthesis/Chapter2.htm

[18] L D Hanke, *Handbook of Analytical Methods for Materials*: Materials Evaluation and Engineering, Inc, **763**, 449-8870 (2009)

[19] http://chemeducator.org/sbibs/s0001005/spapers/15bla897.pdf

[20] A Vilalta-Clement and K Gloystein, *Physics of Advanced Materials Winter School* (2008)

[21] http://www.nano.tm.agilent.com/blog/wp-content/uploads/2007/06/how-an-atomic-force-microscope-works.bmp

[22] http://www.azonano.com/Details.asp?articleID=854

[23] http://www.uksaf.org/tech/xps.html

[24] S P Mbule, MSc. Dissertation, University of the Free state, South Africa (2009)

[25] http://www.chem.qmul.ac.uk/sufaces/scc/scat5_3htm

# CHAPTER 3

# STRUCTURE, MORPHOLOGY AND LUMINESCENT PROPERTIES OF $SrGa_2S_4:Ce^{3+}$ POWDER

## Introduction

*Luminescent properties of strontium thiogallate doped with cerium ($SrGa_2S_4:Ce^{3+}$) have been investigated since the late 19$^{th}$ century. In recent years an intensive study of this material has begun because it is a very attractive photoluminescence (PL), electroluminescence and cathodoluminescence (CL) material for the visible spectral range [1]. In this chapter, the structure, morphology, absorption, photoluminescence and cathodoluminescence characteristics of commercial (from Phosphor Technology, UK) $Ce^{3+}$ doped $SrGa_2S_4$ are reported.*

## 3.1 Experimental procedure

The structure, morphology and luminescent properties of commercial $SrGa_2S_4:Ce^{3+}$ phosphor powder was examined. This phosphor shows bright blue emission under ultraviolet (UV) excitation. Measurements were carried out using various characterization techniques such as X-ray diffraction (XRD), scanning electron microcopy (SEM) and X-ray energy dispersive spectroscopy (EDS). The XRD data was collected over the range $5^o < 2\theta < 70^o$ with a scan rate (for $2\theta$) of $1^o$ per second. The qualitative assessments of the particle morphology were carried out using Shimadzu SSS-550 Super Scan coupled with EDS.

SEM images were recorded at a high energy voltage (15kV) and backscattering mode was used to minimize charging. Images were recorded at 8 000 times, 20 000 times and 48 000 times magnifications. EDS was performed on the lighter grain of the 48 000 times magnification image. PL data was collected in air at room temperature using Varian Cary Eclipse Fluorescence Spectrophotometer with a monochromatized Xenon lamp (60-75 W) and cathodoluminescence (CL) data were recorded using S2000 Ocean Optics Spectrometer. The absorption spectra were recorded using Perkin Elmer Lambda 950 UV-VIS spectrometer. The Labsphere Spectralon® Reflectance Standard over the wavelength range of 250 – 2500 nm was used as reference.

## 3.2 Results and Discussions

### 3.2.1 XRD and SEM/EDS

XRD patterns of a polycrystalline powder obtained from the Phosphor Technology exhibited orthorhombic structure of $SrGa_2S_4$ with diffraction peaks coinciding well with the standard data of JCPDS card No.77-1189 as depicted in Fig. 3.1. XRD crystallography data of $SrGa_2S_4:Ce^{3+}$ lattices are listed in Table 3.1. The experimental values of d-spacing compare reasonably well with theoretical values as shown in Table 3.2. Fig. 3.2 shows (a) 8 000 times, (b) 20 000 times and (c) 48 000 times SEM images of $SrGa_2S_4:Ce^{3+}$ powder. In all the images, the particles were not uniformly distributed and they had irregular shapes. In addition, the particles were highly agglomerated. EDS (Fig. 3.2 (d)) confirmed the presence of the major elements, namely strontium (Sr), gallium (Ga) and sulphur (S). Carbon (C) was also detected and is believed to be coming from carbon tape used for mounting the sample as well as oxygen

which might possibly be coming from the chemisorbed moisture. Kumar et al [2] suggested that the origin of oxygen be studied with controlled oxidation experiments combined with luminescence measurements in future. Chlorine (Cl) is probably from precursors used to prepare this phosphor. $Ce^{3+}$ ions could not be detected most likely due to their relative small concentration in the $SrGa_2S_4$ host matrix.

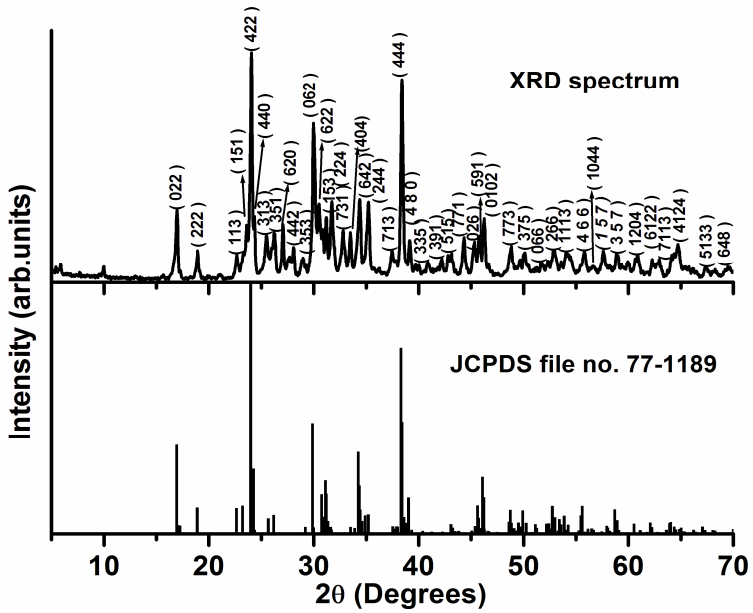


**Fig. 3.1** X-ray diffraction pattern of the $SrGa_2S_4$ host lattice.

Table 3.1

Crystallographic data for $SrGa_2S_4$ lattice

| Phase | Strontium Gallium Sulfide |
|---|---|
| Empirical formula | $SrGa_2S_4$ |
| Structure | Orthorhombic |
| Space group | $D_{2h}^{24}$-Fddd |
| Formula weight | 55.22 g/mol |
| | |
| Lattice parameters | |
| a (Å) | 20.932(6) |
| b (Å) | 20.549(6) |
| c (Å) | 12.227(4) |
| $\alpha = \beta = \gamma = 90^{\circ}$ | |

Table 3.2

h k l planes and d-spacing

| h | k | l | Calculated d-spacing (Å) | Theoretical d-spacing (Å) |
|---|---|---|---|---|
| 0 | 2 | 2 | 5.15 | 5.12 |
| 2 | 2 | 2 | 4.56 | 4.59 |
| 1 | 1 | 3 | 3.84 | 3.84 |
| 1 | 5 | 1 | 3.67 | 3.74 |
| 4 | 2 | 2 | 3.62 | 3.62 |
| 4 | 4 | 0 | 3.56 | 3.58 |
| 3 | 1 | 3 | 3.40 | 3.39 |
| 3 | 5 | 1 | 3.33 | 3.33 |
| 6 | 2 | 0 | 3.20 | 3.23 |
| 4 | 4 | 2 | 3.12 | 3.07 |
| 3 | 5 | 3 | 3.02 | 2.61 |
| 0 | 6 | 2 | 2.91 | 2.91 |
| 6 | 2 | 2 | 2.86 | 2.84 |
| 1 | 5 | 3 | 2.79 | 2.79 |
| 2 | 2 | 4 | 2.74 | 2.75 |
| 7 | 3 | 1 | 2.67 | 2.61 |
| 6 | 4 | 2 | 2.54 | 2.55 |
| 2 | 4 | 4 | 2.48 | 2.49 |
| 7 | 1 | 3 | 2.34 | 2.34 |
| 4 | 4 | 4 | 2.29 | 2.29 |
| 4 | 8 | 0 | 2.24 | 2.25 |
| 3 | 3 | 5 | 2.16 | 2.14 |
| 3 | 9 | 1 | 2.09 | 2.09 |
| 5 | 1 | 5 | 2.05 | 2.05 |
| 7 | 7 | 1 | 2.00 | 2.02 |
| 0 | 2 | 6 | 1.95 | 1.95 |
| 5 | 9 | 1 | 1.93 | 1.93 |
| 0 | 10 | 2 | 1.92 | 1.90 |
| 7 | 7 | 3 | 1.82 | 1.82 |
| 7 | 3 | 5 | 1.78 | 1.78 |
| 0 | 6 | 6 | 1.72 | 1.71 |
| 2 | 6 | 6 | 1.69 | 1.69 |
| 1 | 11 | 3 | 1.65 | 1.65 |
| 10 | 4 | 4 | 1.61 | 1.59 |
| 1 | 5 | 7 | 1.56 | 1.56 |
| 3 | 5 | 7 | 1.53 | 1.53 |
| 12 | 0 | 4 | 1.48 | 1.48 |
| 7 | 11 | 3 | 1.44 | 1.44 |
| 4 | 12 | 4 | 1.40 | 1.40 |
| 5 | 13 | 3 | 1.35 | 1.36 |
| 6 | 4 | 8 | 1.32 | 1.31 |

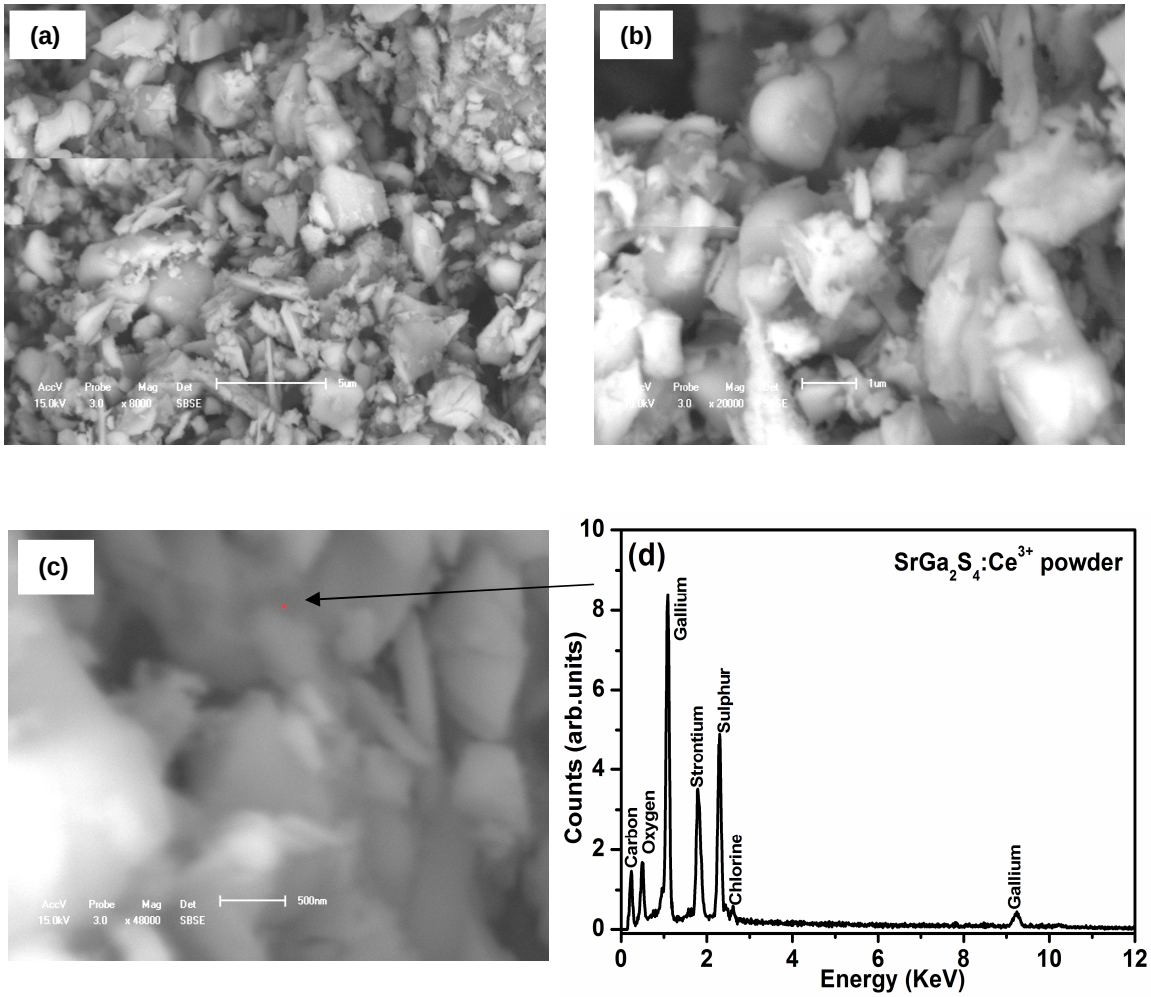


**Fig. 3.2** SEM images of $SrGa_2S_4:Ce^{3+}$ powder **(a)** 8 000 times, **(b)** 20 000 times and **(c)** 48 000 times and **(d)** EDS spectrum.

### 3.2.2 PL and CL

Fig. 3.3 (a) shows the PL (i) emission and (ii) excitation spectra of the $SrGa_2S_4:Ce^{3+}$ powder phosphor. The emission spectrum has two broad bands peaking at 444 nm (2.79 eV) and 485 nm (2.55 eV) which are known to originate from radiative transitions 5d ($T_{2g}$) → 4f ($^2F_{5/2}$) and 5d ($T_{2g}$) → 4f ($^2F_{7/2}$) of $Ce^{3+}$ respectively. The inset is the excitation spectra monitoring 444 nm emission and the excitation wavelength for this emission was 309 nm. The same were obtained when monitoring 485 nm emission peak. Fig. 3.3 (b) shows the schematic diagram of the $Ce^{3+}$ energy levels. $Ce^{3+}$ emission is due to the electronic parity allowed transitions between $5d^1$ ($T_{2g}$) configuration and the $4f^1$ ($^2F$) configuration.

As the $4f^1$ configuration is split by spin-orbits interaction into two levels $^2F_{5/2}$ and $^2F_{7/2}$, one observes two emission bands shifted by about 240 meV and the $5d^1$ configuration is known to split into two levels $E_g$ and $T_{2g}$ in cubic crystal symmetry. The different sides which are occupied by the $Ce^{3+}$ ions could contribute to the broadening of the peaks [3, 4].

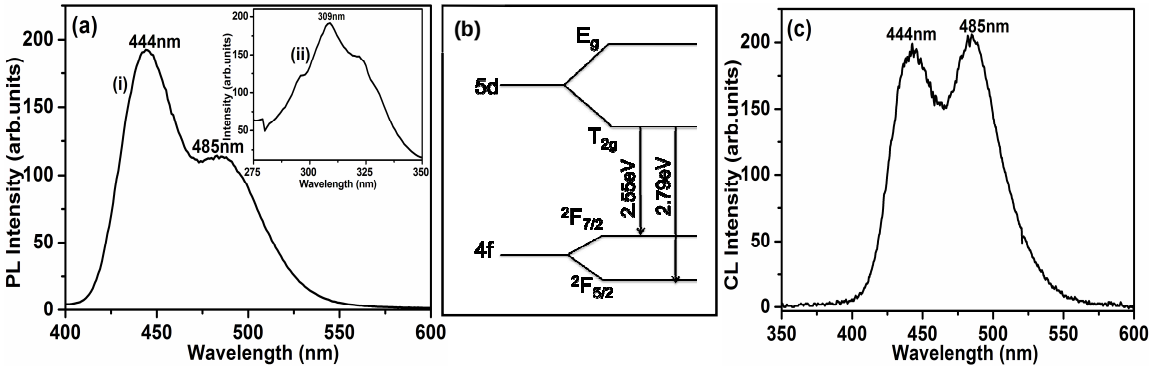


**Figs. 3.3 (a)** (i) PL emission spectra and (ii) excitation spectra of the $SrGa_2S_4:Ce^{3+}$ powder. **(b)** $Ce^{3+}$ energy levels. **(c)** CL emission spectra at a base pressure of 1.3 x $10^{-8}$ Torr (2keV)

Shown in Fig. 3.3 (c) is the CL emission spectra recorded with the electron beam at 2 keV and the vacuum pressure at 1.3 x $10^{-8}$ Torr. The CL spectrum has two broad bands at 444 nm and 485 nm originating from the $Ce^{3+}$ transitions stated above. The emission mechanism for both PL and CL appeared to be the same. CL and PL spectra are closely matching in terms of the wavelength and energy. However, a substantial broadening of the emission spectra in transitions from cathode excitation to photo-excitation was observed as well as the change in the intensity ratio. PL spectrum gives more intense peak at the radiative transition 5d ($T_{2g}$) → 4f ($^2F_{7/2}$) while for the CL spectrum more intense peak is observed at the radiative transition 5d ($T_{2g}$) → 4f ($^2F_{5/2}$).

Always the high energy excitation stimulates the host lattice and direct excitation of the luminescent center (activator) is only possible with UV radiation. Therefore, more charge carriers (electro-hole pair) are generated during electron beam interaction with the crystalline solid or material than with the UV beam interaction. That is, CL from phosphor is a result of the statistics made up of combination of mobile carriers and the luminescence center [5].

Since $Ce^{3+}$ emission is in the 5d - 4f transitions, which are known to be very sensitive to the surrounding ligands because of the 5d states that are directly exposed to the local environment [6]. Because of this kind of behaviour which usually takes place within the band gap of the matrix, a change in the shape, intensity and peak positions of the spectra is observed.

### 3.2.3 UV – VISIBLE ABSORPTION

Fig. 3.4 shows the UV-Vis absorption spectra of $SrGa_2S_4:Ce^{3+}$ powder. The absorption edge of host $SrGa_2S_4$ is situated at about 300nm and these results were previously reported by Zhang Xinman et al [7] and they calculated the band gap and found it to be 4.07eV. The absorption bands situated at around 200 ~ 350 nm may be attributed to the host and the 4f → 5d transition of $Ce^{3+}$ - ions, while the absorption band in the range of 350 ~ 400 nm may only be attributed to the 4f → 5d transitions of $Ce^{3+}$ ions [7].

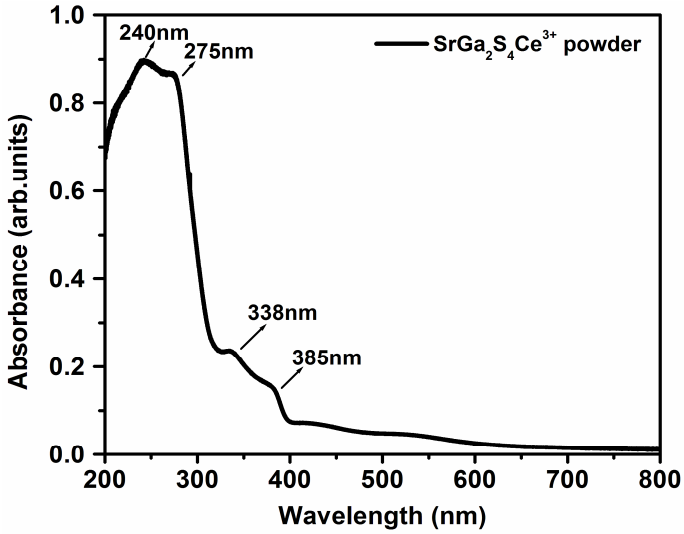


**Fig. 3.4** Optical absorption spectrum of commercial cerium doped strontium thiogallate.

## 3.3 Conclusion

Commercially available $SrGa_2S_4:Ce^{3+}$ powder phosphor was successfully characterized using various techniques. XRD confirmed the orthorhombic structure of $SrGa_2S_4$ that is consistent with the standard JCPDS data. SEM images of the $SrGa_2S_4:Ce^{3+}$ powder showed particles with irregular shapes and EDS detected the presence of the major elements. Both PL and CL showed the broad emission peaks around 444 nm and 485 nm which are due to $Ce^{3+}$ transitions.

## References

[1] M Nazarov, D Y Noh and H Kim, *Material Chemistry and Physics*, **107**, 456-464 (2008).

[2] V Kumar, S S Pitale, V Mishra, I M Nagpure, M M Biggs, O M Ntwaeaborwa and H C Swart, *Journal of Alloys and Compounds*, 21150 (2009).

[3] L Eichenauer, B Jarofke, H C Mertins, J Dreyhsig, W Busse, H E Gumlich, P Benalloul, C Barthou, J Benoit, C Fouassier and A Garcia, *Physica Status Solidi*, **153,** 515 (1996).

[4] A Kato, M Yamazaki, H Najafov, K Iwai, A Bayramov, C Hidaka, T Takizawa and S Iida, *Journal of Physics and Chemistry of Solids*, **64**, 1511-1517 (2003).

[5] L Ozawa and M Itoh, *Chemical Review*, Vol **103**, No.10, 3836-3855 (2003).

[6] J Li, O H Y Zalloum, T Roschuk, C L Heng, J Wojcik and P Mascher, *Advances in Optical Technologies*, 1-10 (2008)

[7] Z Xinman, W Hao, Z Heping and S Qiang, *Journal of Rare-Earths*, **25**, 701-705 (2007).

# CHAPTER 4

# CATHODOLUMINESCENCE DEGRADATION OF $SrGa_2S_4:Ce^{3+}$ POWDER

## Introduction

*A primary focus of the current research in the area of display phosphors is directed towards efficient phosphor development to be used in new generation of low–voltage excitation (≤ 5keV) for flat-panel displays such as field emission display (FED). In the present study, commercial $SrGa_2S_4:Ce^{3+}$ powder phosphor was investigated for possible application in low voltage FEDs. Cathodoluminescence (CL) properties of this phosphor were investigated at various accelerating voltages (1.5 - 2.5 kV) and oxygen pressures ($7.5 \times 10^{-7}$ Torr $O_2$ - $1.3 \times 10^{-8}$ Torr) to determine their effects on the CL intensity when the samples were irradiated with a beam of electrons at 2keV. X-ray photoelectron spectroscopy (XPS) and Auger electron Spectroscopy (AES) were used to analyze the chemical compositions and electronic states of the elements present in $SrGa_2S_4:Ce^{3+}$ phosphor before and after degradation.*

## 4.1 Experimental procedure

A combination of techniques such as (XPS), (AES) and CL spectroscopy were used to investigate the surface chemical changes and degradation of the CL intensity when the $SrGa_2S_4:Ce^{3+}$ powder was irradiated with high energy beam of electrons. The electron beam current was maintained at 12 µA and the accelerating voltage was varied from 1.5 to 2.5 kV. The Auger and CL data were collected in a vacuum chamber with a base pressure of $1.3 \times 10^{-8}$ Torr. Afterwards the chamber was backfilled with oxygen gas to $7.5 \times 10^{-7}$ and $1.0 \times 10^{-7}$ Torr. The Auger and CL data were collected using the same primary electron beam. The PHI (model 549) Auger spectrometer and S2000 Ocean Optics spectrometer were used simultaneously to collect the Auger and CL data respectively. The decrease of the CL intensities of the 444 nm and 485 nm peaks of $Ce^{3+}$ were monitored continuously for 8 hours**.**

The XPS data were collected from both undegraded (unirradiated) and electron beam degraded powder samples using the PHI 5000 Versa probe-Scanning ESCA microprobe. $Ar^+$ ion gun with a sputter rate of about 85Å/min was used to minimize charging on the surface when using a monochromatic AlKα radiation as the excitation source. A 25 W and 15 kV energy x-ray beam at 100 µm diameter was used to analyze Sr 3d, O 1s, Ga 2p and S 2p binding energy peaks (pass energy 11 eV, analyzer resolution $\leq$ 0.5 eV). Multipak (version 8.2) software [1] was used to identify chemical elements and their electronic states. To determine the residual gases present in the vacuum chamber of the Auger spectrometer, residual gas analyses were performed by Anavac-2 residual gas analyzer (RGA).

## 4.2 Results and Discussions

### 4.2.1 RESIDUAL GAS ANALYSIS

Residual gas analyzer (RGA) was performed to determine the different gas species which were possibly present in the ultra high vacuum (UHV) chamber of the AES system. The basic principle of RGA is to create a beam of ions from the samples of the gas molecules being analyzed. This result in a mixture of ions which are later separated into individual species through their charge-to-mass ratios. Fundamentally, samples are irradiated with a high energy electron beam and the molecules of the gases present in the chamber will be ionized.

Therefore, a hot emission filament generates this ionizing electron beam and it is extracted by means of an electric field [2]. The RGA spectra taken before and after degradation at different oxygen pressures are shown in Fig. 4.1. RGA measurements were performed before degradation with the beam on and off and after degradation with the beam on. Fig. 4.1 (a) shows the intensities of different gases present in the UHV chamber before degradation when the Auger vacuum chamber was at a base pressure of 1.3 x $10^{-8}$ Torr.

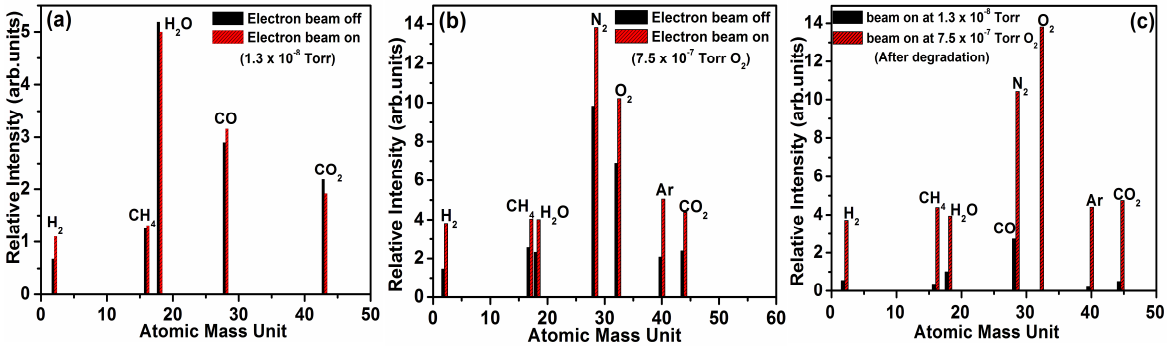


**Fig. 4.1** RGA spectra taken before degradation in an Auger UHV chamber of a pressure of **(a)** 1.3 x $10^{-8}$ Torr and later backfilled with oxygen to **(b)** 7.5 x $10^{-7}$ Torr $O_2$. **(c)** RGA results after degradation with the electron beam on at various oxygen pressures.

RGA spectra shown in Fig. 4.1 (a) above, confirmed the presence of residual gases such as hydrogen ($H_2$), carbon monoxide (CO), carbon dioxide ($CO_2$), water vapour ($H_2O$) and methane ($CH_4$) in the vacuum system. An increase in the intensity of $H_2$, $CH_4$ and CO gases was observed as the electron beam was switched on and a decrease in the intensity of $H_2O$ and $CO_2$. It is believed that during the interaction of the sample with the electron beam, surface chemical reactions take place and this phenomenon can be explained by an electron stimulated surface chemical reactions (ESSCR) model proposed by Holloway et al [3]. According to this model, the electron beam can ionize these gases into more volatile species resulting in the formation of new compounds following chemical reactions between the volatile species.

Fig. 4.1 (b) shows the RGA spectra taken after oxygen was leaked into the system. The chamber was backfilled with oxygen to 7.5 x $10^{-7}$ Torr $O_2$. The same gases detected previously at a base pressure were still present except for additional atmospheric gases such as Ar, $N_2$ and $O_2$. The results in Fig. 4.1 (b) indicate the lower intensity for gases when the electron beam is off and an increase or higher intensity of the gases when the beam is on. The increase in the concentration

of the gases when the beam is switched on is due to the de-gassing from the sample material ($SrGa_2S_4:Ce^{3+}$) during its interaction with the beam of electrons. Shown in Fig. 4.1 (c) is the relative RGA results for measurements taken after degradation at a base pressure of 1.3 x $10^{-8}$ Torr and oxygen pressure of 7.5 x $10^{-7}$ Torr $O_2$ with the electron beam on. It is evident from Fig. 4.1 (c) that all gases that were present at a base pressure of 1.3 x $10^{-8}$ Torr (Fig. 4.1 (a)) before degradation when the beam was on decreased in intensity after degradation, except for a small amount of Ar gas which was detected.

At 7.5 x $10^{-7}$ Torr $O_2$ pressure, no changes were observed in $H_2$ and $H_2O$ intensity after degradation as compared to before degradation when the beam was on (Fig. 4.1 (b)) and as for $CH_4$ and $CO_2$ a slight increase was observed. A fairly large increase in $O_2$ intensity after degradation was observed and a decrease in $N_2$ intensity as well as a slight decrease in Ar gas intensity. A general increase was observed for all gases after degradation at 7.5 x $10^{-7}$ Torr $O_2$ pressure than to gases at base pressure (1.3 x $10^{-8}$ Torr) as shown in Fig. 4.1 (c). This is due to desorption of oxygen containing species in the system as a result of reaction of $O_2$ with element such as C and S forming volatile $CO_2$ and $SO_2$.

Although there was a decrease in the intensity of the water vapour at a base pressure (1.3 x $10^{-8}$ Torr), it is apparent from all spectra that the amount of water vapour still dominates other gases in the chamber. The electron beam can break up the $H_2O$ molecules into $2H^+$ and $O^-$ ions, thereby creating a high concentration of re-active atomic species at the surface of the phosphor material. These species may combine chemically according to the ESSCR model and form new compounds that can decrease the CL intensity of phosphor materials, thereby accelerating degradation process [4]. That is, $2H^+$ and $O^-$ ions can react with sulfur (S) from the target material or adventitious carbon (C) from the chamber to form gases such as $H_2S$ and $CO_2$.

### 4.2.2 CL INTENSITY DEGRADATION

Fig. 4.2 (a) is the AES spectrum recorded before and after degradation at an oxygen pressure of 7.5 x $10^{-7}$ Torr. The Auger peak positions of individual element(s) detected on the surface are clearly indicated. In the low energy region 40-120 eV, the Sr and Ga MNN Auger transitions overlap. A change in peak shape for Sr Auger transitions could, however be observed after 500 $C.cm^{-2}$ of electron dose after ageing as indicated in the stand alone inset figure in Fig. 4.2 (a).

A decrease in the surface oxygen concentration together with the removal of adventitious C was also observed. A significant decrease in S after degradation was observed due to its high volatility. The AES observations correlates with the Auger peak to peak heights (APPHs) shown as a function of electron dose in Fig. 4.2 (b).

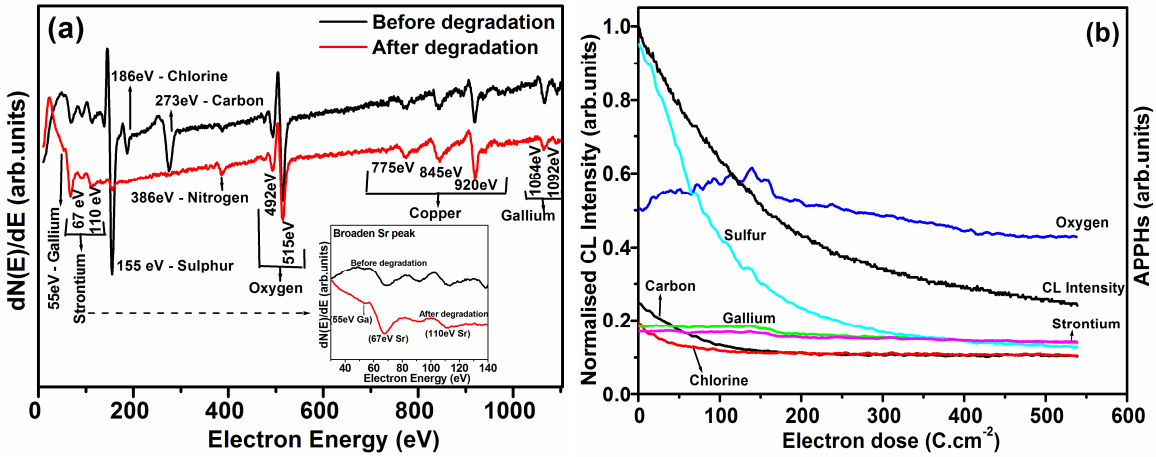


**Fig. 4.2 (a)** AES spectra of $SrGa_2S_4:Ce^{3+}$ powder before and after ageing **(b)** APPHs as a function of Coulomb loading at 7.5 x $10^{-7}$ Torr $O_2$ pressure (beam voltage = 2 kV).

The Cl present is properly from precursors used to prepare the sample. Cu peaks detected at positions 775, 845 and 920 eV arises from the Cu sample holder. The presence of Cu peaks before and after degradation clearly indicates that the electron beam was not hitting directly on the sample, but small portions of beams were also on to the sample holder. In order to avoid charging, the incident beam is not placed directly on the sample. Thus, some of the electrons will fall on the holder. The Auger spectrum recorded after electron beam ageing shows a non-distinctive emergence of the low energy Ga peak due to the admixture with Sr Auger transitions as mentioned above. For the high energy Ga Auger LMM transitions before ageing located at 1067 eV, a shift of 3 eV as well as a decrease in the peak height was observed after the ageing process suggesting charging to be taking place on the surface.

The APPHs in Fig. 4.2 (b) show a slight increase in O up to 150 $C.cm^{-2}$ loading which thereafter gets stabilized. This may be due to the volatile S and C atoms coupling under electron stimulation with the chamber $O_2$ to form S-O and C-O molecular species which later leaves the system. RGA in Fig. 4.1 (b) reveals that the residual gas level inside the chamber was dominated by $N_2$ in the background atmosphere before ageing and $O_2$ during ageing while leaking $O_2$ into

the vacuum chamber together with traces of $H_2$, $H_2O$, CO and $CO_2$ species. Dissociated surface-physisorbed molecular species (e.g., $H_2O$, $H_2$ or $O_2$) by the electron beam are converted to reactive atomic hydrogen and oxygen, which combine with S and C on the surface, forming volatile sulfur and carbon compounds, such as $SO_x$ or $H_2S$, CO or $CO_2$ which desorbed from the surface [5].

Degradation was also performed at 1.3 x $10^{-8}$ Torr and 1.0 x $10^{-7}$ Torr $O_2$ pressures and the results exhibited similar trend of Auger peaks observed at 7.5 x $10^{-7}$ Torr $O_2$, except for oxygen (O) which was observed to be increasing at a base pressure of 1.3 x $10^{-8}$ Torr due to large percentage area contribution observed from the XPS data of oxide layer formed on the surface at this pressure. In addition, at base pressure (1.3 x $10^{-8}$ Torr) the degradation was done by changing the beam voltage from 1.5 to 2.5 kV and still no drastic changes were observed on the trend of major elements (Sr, Ga and S).

Fig. 4.3 (a) shows the CL spectra recorded before and after ageing at oxygen pressure of 7.5 x $10^{-7}$ Torr with 2 kV electron beam. The effects of various oxygen pressures were investigated on the degradation characteristics of the $SrGa_2S_4:Ce^{3+}$ powder phosphor. Fig. 4.3 (b) compares the decrease in the CL intensity as a function of electron dose at different vacuum pressure.

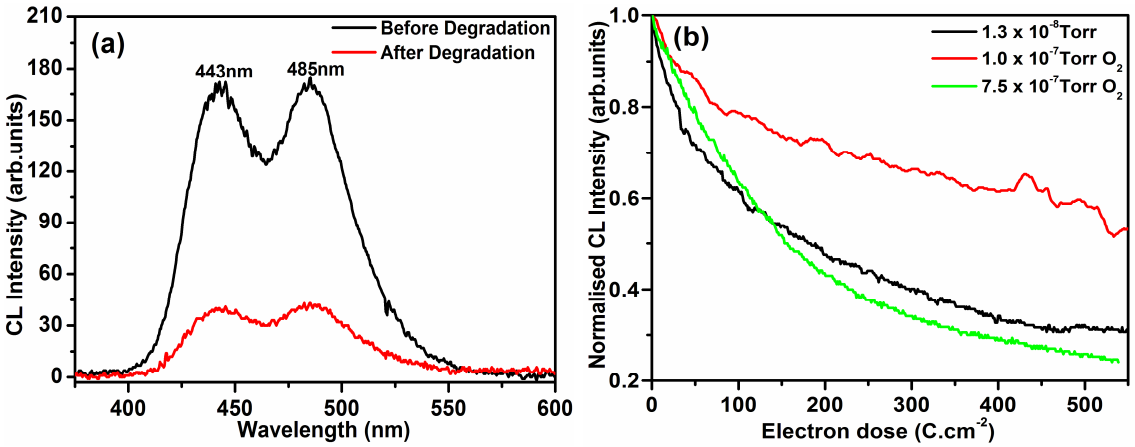


**Fig. 4.3 (a)** CL emission of the $SrGa_2S_4:Ce^{3+}$ powder before and after ageing at 7.5 x $10^{-7}$ Torr $O_2$. **(b)** Normalized CL intensity as a function of electron dose of $SrGa_2S_4:Ce^{3+}$ powder at various oxygen pressures.

The CL emission spectra, as shown in Fig. 4.3 (a) has two broad bands with maxima at 443 nm (2.79 eV) and 485 nm (2.55 eV) which are well known to originate from radiative transitions

5d ($T_{2g}$) to 4f ($^2F_{5/2}$) and 5d ($T_{2g}$) to 4f ($^2F_{7/2}$) respectively of the $Ce^{3+}$- ion. In Fig. 4.3 (b), are the normalized CL degradation curves against the electron dose at various oxygen pressures. Almost the same pattern of CL degradation curves were observed for the degradation of the $SrGa_2S_4:Ce^{3+}$ powder performed at 1.3 x $10^{-8}$ Torr and 7.5 x $10^{-7}$ Torr $O_2$ pressures. The decrease of the CL intensity degradation was observed to be fast at a base pressure (1.3 x $10^{-8}$ Torr) and fastest at 7.5 x $10^{-7}$ Torr $O_2$, but a rapid decrease in the CL intensity within the first few seconds was observed at 7.5 x $10^{-7}$ Torr $O_2$ and thereafter the intensity continued to decrease with increasing electron dose.

In this study, the rate of degradation was not slow at a base pressure as anticipated, instead it was observed to be slowest at 1.0 x $10^{-7}$ Torr $O_2$ which indicates a different nature of reactions on the surface. From the APPHs taken at 1.0 x $10^{-7}$ Torr $O_2$ which is the same as the one shown in Fig. 4.2 (b), initially there was an increase in both the Sr and O content in the same region up to 150 $C/cm^2$ electron dose signifying the formation of SrO overlayer. After this region a decrease in Sr content was observed indicating a loss of Sr bonded in Sr-S and Sr-Sr species of $SrGa_2S_4$. The same observation is correlated to the XPS 3d spectra of Sr from Fig. 4.4 (a) and (d) where SrO was detected in trace amount before degradation and later developed into significant contribution (24.3%) after degradation at positions 135.2 eV and 137.0 eV respectively. The XPS (Sr 3d spectrum) results at base pressure (1.3 x $10^{-8}$ Torr) revealed a prominent percentage (37.6%) of formation of SrO after degradation.

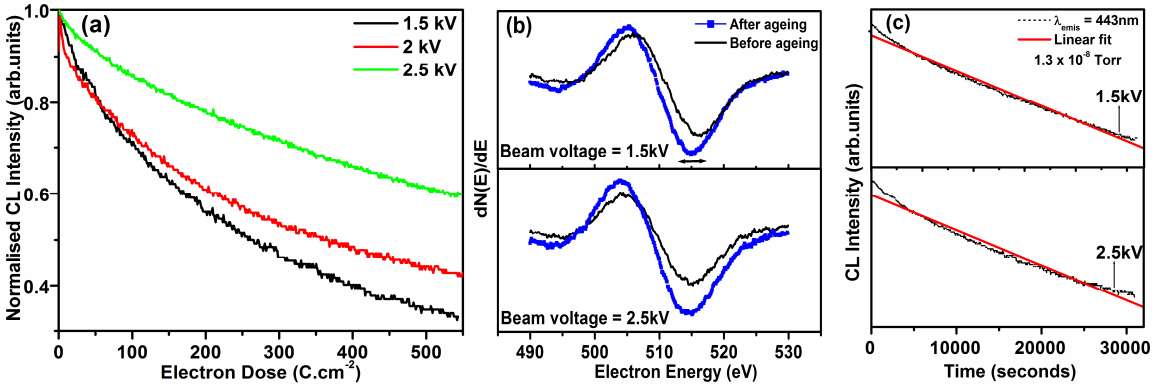


**Figs. 4.4 (a)** Ageing characteristics at various accelerating voltage at a background pressure of 1.3 x $10^{-8}$ Torr and **(b)** Auger profiles of $O_2$ recorded before and after ageing with different accelerating voltage of primary electron beam at base pressure of 1.3 x $10^{-8}$ Torr. **(c)** Linear fits for the $SrGa_2S_4:Ce^{3+}$ powder at 1.5 and 2.5 kV electron beam voltage.

The effect of different anode voltages on the sustainability of CL output was also monitored and the results are shown in Fig. 4.4 (a). Since, the operational voltage requirements of FEDs have changed from low voltages (≤ 2 kV) to moderate voltages (2-10 kV), because carbon nanotube (CNT)-FEDs use higher voltage e-beams than Spindt-type FEDs, it becomes imperative to observe the CL ageing behavior on the high and low side of the limiting value of the anode voltage (i.e. 2 kV). It can be seen from Fig. 4.4 (a) that at 2.5 kV the phosphor requires more than 500 $C.cm^{-2}$ of Coulomb loading to decay to 50% of its initial CL output whereas at other beam voltages, a severe degradation rate is observed. This is attributed to the charging phenomena as depicted (Fig. 4.4 (b)) from shift in the minimum of the derivate $O_2$ Auger signal before and after the ageing process.

Also the role of ionization cross section cannot be denied in the present case [6]. A new electron distribution results from the collisions of electrons with gas molecules or atoms. A collision occurs when the electron passes within a characteristic area around the particle known as the total cross section $\sigma_T$. With each collision, the electron may lose some energy $\Delta E$ and become scattered at an angle $\theta$ away from the initial direction. This effect commonly called as skirting is resolved at higher accelerating voltages and may slow down the rate of degradation.

Shown in Fig. 4.4 (c) are the plots of the slopes of the CL intensity degradation curves only at 1.5 and 2.5 kV beam voltages with a pressure of $1.3 \times 10^{-8}$ Torr. The slopes of the curves were determined using the Origin 6.0 software. In Table 4.1 (a) and (b) is the CL degradation curves life-times parameters at various oxygen pressures and accelerating voltages.

Table 4.1 (a)

| PRESSURE (Torr) | $1.3 \times 10^{-8}$ | $1.0 \times 10^{-7}$ | $7.5 \times 10^{-7}$ |
|---|---|---|---|
| LIFE-TIME (hrs) | 19.1 | 41.9 | 14.6 |

(b)

| BEAM VOLTAGE (kV) | 1.5 | 2.0 | 2.5 |
|---|---|---|---|
| LIFE TIME (hrs) | 19.2 | 39.4 | 41.1 |

The CL degradation curves were fitted using logarithmic scale linear fit whereby the intensity of the luminescence is given by:

$$\log\left(\frac{I}{I_o}\right) = -\frac{t}{\tau} \text{ , where} \quad (4.1)$$

$I_o$ is the initial CL intensity, $I$ is the CL intensity, $\tau$ is the relaxation time, a constant for the material and $t$ is the time. After time t, the intensity of the luminescence is reduced from $I_o$ to $I$. Equation (1) can be written as:

$$\frac{I}{I_o} = e^{(-t/\tau)} \quad (4.2)$$

Taking the logarithm on both sides, we get:

$$\log I = \log I_o + \left(\frac{-1}{\tau}\right)t \quad (4.3)$$

Equation (3) can be re-written as:

$$y = c + mx \quad (4.4)$$

whereby, $m = \frac{-1}{\tau}$ and $c = \log I_o$ (4.5)

Looking at the calculated half-life times in Table 4.1 (a), it is evident that at 7.5 x $10^{-7}$ Torr $O_2$ (14.6hrs) and 1.3 x $10^{-8}$ Torr (19.1hrs) pressures, the decay times values were shorter in comparison to the pressure 1.0 x $10^{-7}$ Torr $O_2$, indicating a rapid degradation rate at these pressures. In Table 4.1 (b), the half-life times range from smaller value (19.2hrs) at lower accelerating voltage to a higher value (41.1hrs) at increased accelerating voltages showing that as the electron beam voltage is increased, the rate of decay with respect to time becomes slower.

### 4.2.3 XPS ANALYSIS

The XPS results for undegraded and degraded spots of $SrGa_2S_4:Ce^{3+}$ powders are shown in Figs. 4.5 (a) to (f). The XPS 3d spectrum of Sr (undegraded) shown in Fig. 4.5 (a) has two peaks of Sr-S and two peaks of Sr-Sr and/or $SrSO_4$ bonds, $3d_{3/2}$ and $3d_{5/2}$ existing within the $SrGa_2S_4$:Ce phosphor. The metallic bonding may be arising from the interstitial Sr or surface terminated Sr sites. After the ageing process additional signatures corresponding to Sr-O bonding belonging to the SrO compound are observed together with a decrease in the Sr peaks of $SrGa_2S_4$ (as evident from the decrease in their relative contribution). The $2p_{3/2}$ component of S-Sr and S-Ga bonding in $SrGa_2S_4$ is represented by a peak at 160.2 eV and 162.5 eV before electron bombardment respectively. After ageing, a noteworthy (although very small) change that appeared on the surface was the appearance of the S peak at 169 eV corresponding to the S-Sr bonding in a $SrSO_4$ compound [1].

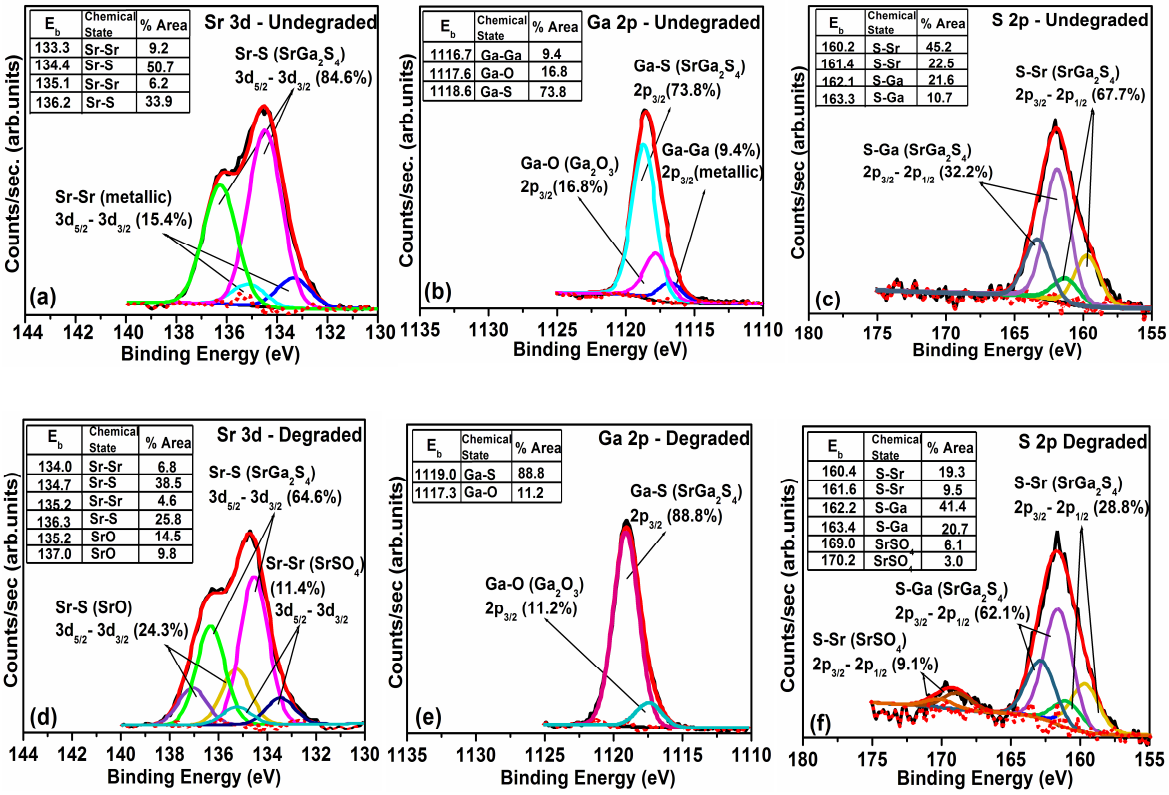


**Figs. 4.5 (a-f)** XPS high resolution scans and fitting results for (a, b & c) undegraded regions (before ageing) and (d, e & f) degraded (after ageing) regions of the $SrGa_2S_4:Ce^{3+}$ powder phosphor.

For the Ga XPS spectra before and after degradation, it is observed that the metallic Ga signal disappeared after the degradation and also the relative contribution of Ga-S bond in $SrGa_2S_4$ increased. This observation correlates with the slight decrease in Ga APPHs in Fig. 4.2 (b) during electron bombardment. It was previously found that oxygen ions substitute some of the S ions that form a bonding with the Ga ion in the $SrGa_2S_4$ matrix itself [7]. So the Ga-O bond comes from the lattice itself. Overall, from the XPS results it is clear that ESSCRs occurred on the surface whereby SrO and traces of $SrSO_4$ formed under electron bombardment in the $O_2$ ambient. The product from the beam-gas and the signal-gas interactions may modify these reactions or even initiate new reactions. The presence of non-luminescent SrO may well contribute to the loss in CL brightness.

Depicted in Fig.4.6 is an illustration of possible ageing mechanism of the $SrGa_2S_3:Ce^{3+}$ powder during the degradation process in the presence of oxygen.

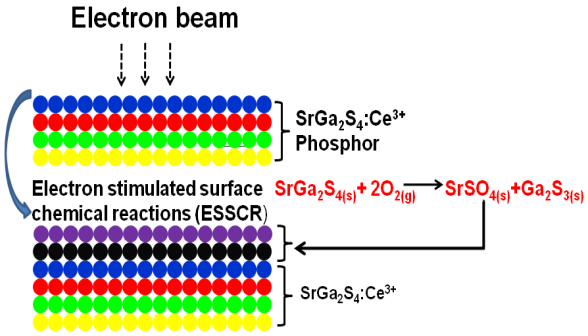


**Fig. 4.6** Illustration of possible chemical reaction(s) taking place on the surface according to ESSCR.

During the interaction of the electron beam with the target material ($SrGa_2S_3:Ce^{3+}$), surface reactions take place, thus resulting in new layers (non-luminescent and less luminescent) formed on the surface which are known to stimulate degradation process and decrease the CL intensity [8]. In this study, oxygen induced layers such as $SrSO_4$, SrO and $Ga_2O_3$ were formed on the surface as revealed by the XPS. Equations below are possible half-reactions by which these formations can form:

$$Sr^{2+} + SO_4^{2-} \rightarrow SrSO_4 \quad \ldots\ldots\ldots\ldots\ldots\ldots \ldots\ldots \Delta H = -1453.1 kJ/mol$$

$$Sr^{2+} + O^{2-} \rightarrow SrO \quad \ldots\ldots\ldots\ldots\ldots\ldots\ldots\ldots \Delta H = -592.0 kJ/mol$$

$$Ga^{3+} + 2O^{2-} \rightarrow Ga_2O_3 \quad \ldots\ldots\ldots\ldots\ldots\ldots\ldots\ldots \Delta H = -1089.1 kJ/mol$$

Enthalpies of formations [9] are also shown and all values are negative suggesting that these reactions are thermodynamically possible.

## 4.3 Conclusion

It can be concluded from the present work that physico-chemical reactions occurred on the surface of the $SrGa_2S_4:Ce^{3+}$ powders under prolonged electron beam bombardment. The ageing characteristics were found to be dependent on the primary beam accelerating voltages. By allowing $O_2$ gas around the specimen, the number and type of reactions are multiplied leading to a faster ageing process.

Numerous factors such as scattering of the primary beam, modification of the gas due to the creation of positive and negative ions, dissociation products and excited molecules aiding to the formation of volatile surface entities, constitute and govern the overall ageing mechanism for $SrGa_2S_4$ phosphor. An SrO surface overlayer formation is clearly indicated.

The study brings forth two important requisites for the applicability of this phosphor in displays: (a) the use of low to moderate (2-5 kV) electron beam excitation and (b) a surface protection to inhibit the growth of non-luminescent oxide and sulfate layers.

## References

[1] J F Moulder, W F Stickle, P E Sobol and K D Bomben, *Handbook of X-Ray Photoelectron Spectroscopy*, *Perkin-Elmer,* Eden Prairie, MN, USA (1992).

[2] M M Biggs, MSc. Dissertation, University of the Free State, South Africa (2009).

[3] P H Holloway, T A Trottier, J Sebastian, S Jones, X M Zhang, J S Bang, B Abrams, W J Thomes and T J Kim, *J. Appl. Phys.* **88** 1 (2000).

[4] S P Mbule, MSc. Dissertation, University of the Free State, South Africa (2009).

[5] B L Abrams, W D Roos, P H Holloway and H C Swart, Surf. Sci. **451**, 174 (2000).

[6] H C Swart, L Oosthuizen, P H Holloway and G L P Berning, *Surf. Interface Anal.* , **26** (5) 337 (1998).

[7] Y Izumi, S Okamoto, K Tanaka and Y Inoue, Jpn. J. Appl. Phys., **38**, 4798 (1999).

[8] H C Swart, J J Terblans, E Coetsee, V Kumar, O M Ntwaeaborwa, M S Dlamini and J. J. Dolo, *Surface Interface Analysis,* **42**, 922 (2010).

[9] D R Lide, *Handbook of Chemistry and Physics,* 89$^{th}$ edition (2008-2009).

# CHAPTER 5

# $SrGa_2S_4:Ce^{3+}$ THIN FILM GROWTH, STRUCTURE, MORPHOLOGY, TOPOGRAPHY AND LUMINESCENT PROPERTIES

## Introduction

*Thin films of $SrGa_2S_4:Ce^{3+}$ phosphor are promising for full colour electroluminescence (EL) and field emission displays (FED) because of the phosphor's good optical properties [1]. These films were previously prepared using several different techniques such as Rutherford sputtering (RF), molecular beam epitaxy (MBE), reactive multi-source deposition (MSD), deposition from binary depositions (DVB), reactive multisource deposition and Pulsed Laser Deposition (PLD). In this study, luminescent properties of thin films of $SrGa_2S_4:Ce^{3+}$ phosphor deposited on Silicon (Si) (100) substrate using pulsed reactive cross laser-beam ablation (PRCLA) technique are reported. The structure, morphology, topography, as well as the photoluminescence and cathodoluminescence characteristics of $SrGa_2S_4:Ce^{3+}$ thin films are also reported.*

## 5.1 Experimental procedure

Silicon (Si) (100) substrates were first cleaned with KIMTECH SCIENCE KIMWIPES obtained from Kimberly Clark Professionals. A pellet with a 2.4 cm diameter and 6 mm thickness was prepared by pressing the $SrGa_2S_4:Ce^{3+}$ powder for 1hour at a pressure of 1.96 x $10^7$ mbar. The pellet was then annealed for 6 hours at 600°C temperature in vacuum to improve its hardness. It was then mounted on a rotating holder lying diagonally to a heater on which Si substrates were mounted for ablation. The distance between the target and the substrates was maintained at 4 cm during the deposition of each film.

The Lambda Physik EMG 203 MSC 309 nm XeCl excimer laser was used to ablate the target. The film growth was carried out in a chamber which was first evacuated to a base pressure of 8 x $10^{-5}$ mbar before backfilling to pressures of 1.0 x $10^{-2}$ mbar Ar and 1.0 x $10^{-2}$ mbar $O_2$, where Ar and $O_2$ were used as pulse cross gases. The films were deposited at different substrate temperatures ranging from 400°C to 600°C with 28 800 and 57 600 pulses respectively. The laser beam was operated at 8 Hz repetitive rate. The substrate temperature, number of pulses and the working pressure were varied during the preparation of the thin phosphor films.

Characterization of the films was carried out with scanning electron microscopy (SEM), atomic force microscopy (AFM) and x-ray diffraction (XRD). Cathodoluminescence (CL) and photoluminescence (PL) data were recorded with S2000 Ocean Optics Spectrometer and Varian Cary Eclipse Fluorescence Spectrophotometer respectively. Auger electron spectroscopy (AES) was used to analyze the elemental (chemical) composition.

## 5.2 Results and Discussions

### 5.2.1 XRD

Figs. 5.1 (a), (b) and (c) shows the XRD patterns and the Miller indices of the $SrGa_2S_4:Ce^{3+}$ films prepared at different substrate temperatures, number of pulses and cross pulse gases respectively. A highly crystalline $SrGa_2S_4$ layer was observed at the growth temperature of 400°C. From the comparison with the standard powder pattern of $SrGa_2S_4$ (JCPDS file no. 77-1189) all peaks as indicated in Fig. 5.1 (a)-(i), were found to belong to orthorhombic $SrGa_2S_4$ crystal structure, except for an identified impurity peak (marked x) at $2\theta = \sim 47^o$.

The diffraction peak (10 4 4) became more strong as compared to the (10 4 4) powder diffraction peak in Chapter 3.

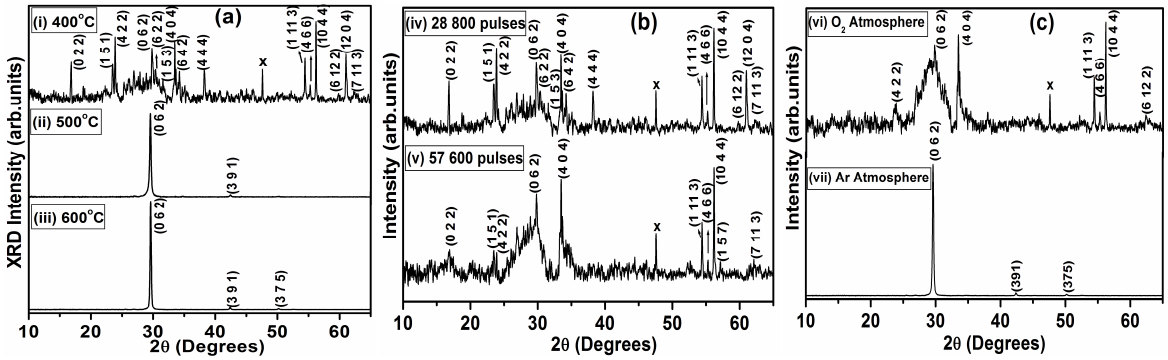


**Fig. 5.1** The XRD diffraction patterns of the $SrGa_2S_4:Ce^{3+}$ films deposited at different **(a)** substrate temperatures, **(b)** no. of pulses, and **(c)** cross pulse gases.

A preferential growth along the orientation (0 6 2) was observed when the substrate temperature was increased to 500°C and 600°C. In addition, small signatures of (3 9 1) and (3 7 5) peaks which also belong to the orthorhombic $SrGa_2S_4$ crystal structure were detected. Similar results as the once observed at 400°C and 500°C substrate temperatures were reported by Hannele Heikkinen et al [2].

The XRD patterns in Fig. 5.1 (a) shows that the film growth is sensitive to the substrate temperature. The intensity of the (0 6 2) peak was observed to increase with an increase in the substrate temperature from $T_{substrate}$ = 400°C to $T_{substrate}$ = 600°C. These results also indicate that crystallinity can be achieved even without post-deposition annealing. K Tanaka et al [3] investigated the crystallinity of $SrGa_2S_4:Ce^{3+}$ thin films grown on quarts glass substrates by MBE technique. The films were grown at substrate temperature of 400°C to 600°C. They reported a gradual decrease in the XRD peak intensity at $T_{substrate}$ > 600°C and $T_{substrate}$ < 500°C and found the best substrate temperature for $SrGa_2S_4$ growth to be around 560°C. T. Yang et al [4] reported the same substrate temperature as the best for $SrGa_2S_4$ films growth.

Shown in Fig. 5.1 (b) are the XRD patterns of the $SrGa_2S_4:Ce^{3+}$ films deposited at 28 800 and 57 600 numbers of pulses. A perfect match of the peaks (4 0 4), (1 11 3), (1 5 3) and (10 4 4) corresponding to the diffraction of $SrGa_2S_4$ powder phosphor were observed in both films. The peak along the orientation (10 4 4) was again observed in both films to be very intense.

The diffractions peaks along the (0 2 2), (1 5 1), (4 2 2), (0 6 2), (6 2 2), and (4 6 6) orientations became weak as the number of pulses were increased to 57 600 (Fig. 5.1 (b)–(v)) with the broadening of the (0 6 2), (4 2 2) and (4 0 4) peaks probably due to poor crystallinity. The (1 5 7) and (7 11 3) peaks became strong as a result of increasing number of pulses. It was therefore concluded that an increase in number of pulses affects the phase purity of the material, in turn disrupting the crystallinity.

Fig. 5.1 (c) shows the XRD patterns of $SrGa_2S_4$ films deposited in Ar and $O_2$ environment. The peaks corresponding to the diffraction of $SrGa_2S_4$ were observed (Fig. 5.1 (c)-(vi)). The main peaks (4 2 2), (4 0 4) and (0 6 2) of $SrGa_2S_4$ became weak in $O_2$ environment and were less crystalline and the peak along the (4 0 4) orientation was observed to become stronger but still with poor crystallinity. The strong peak along the orientation (10 4 4) was again observed in this case.

### 5.2.2 ELEMENTAL COMPOSITION AND PARTICLE MORPHOLOGY

Fig. 5.2 (a) shows the SEM image of the surface of the $SrGa_2S_4:Ce^{3+}$ film deposited at 400°C substrate temperature. The image shows a smooth film with small and bigger spherical particles distributed unevenly on the surface. Similar morphology was observed from the SEM images of the films deposited at different conditions. Shown in Fig. 5.2 (b) is the Auger survey spectrum of the same film. All major elements of $SrGa_2S_4:Ce^{3+}$ were detected from all the films. In addition, atmospheric O and C were also detected.

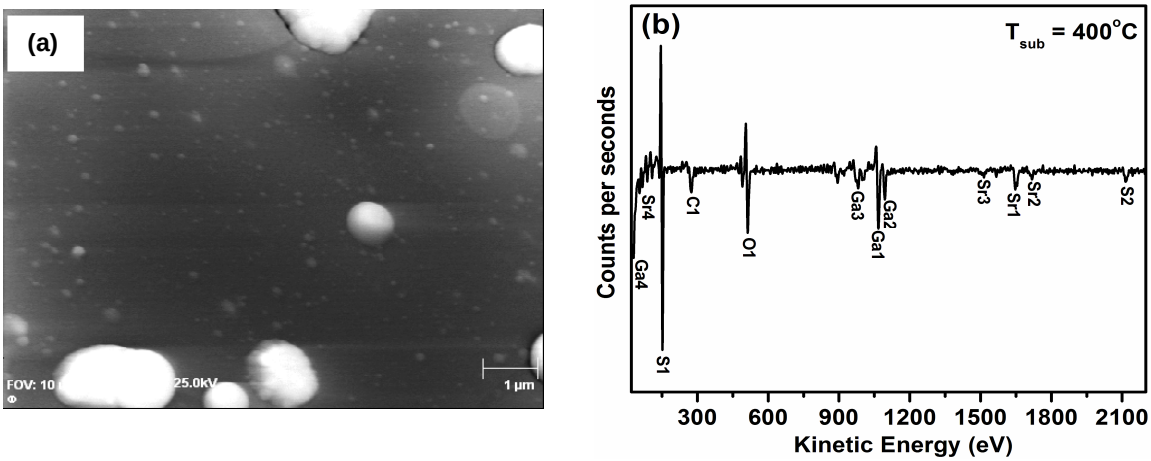


**Fig. 5.2 (a)** The SEM micrograph and **(b)** Auger survey spectrum of the $SrGa_2S_4:Ce^{3+}$ film deposited at 400°C.

### 5.2.3 SURFACE TOPOGRAPHY

Figs. 5.3 (a) – (c) and (d) – (f) show respectively the AFM images of the films deposited at the substrate temperatures of 400, 500, and 600$^{o}$C before and after annealing at 700$^{o}$C in vacuum.

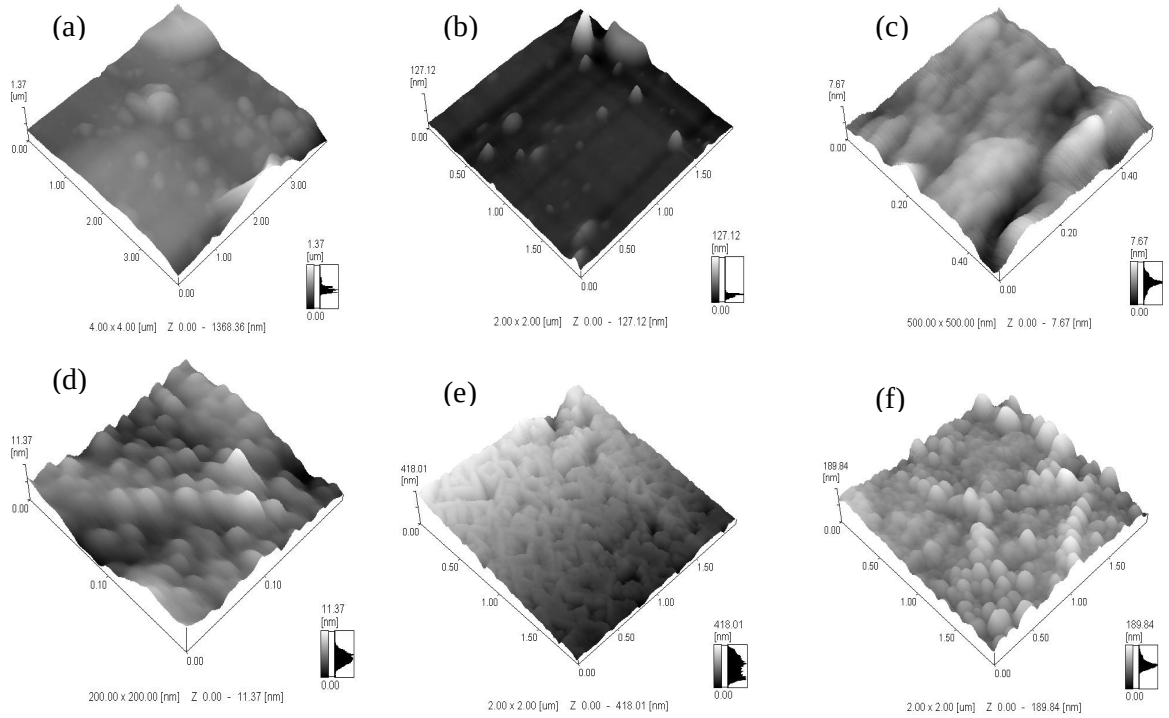


**Fig. 5.3** AFM images for the unannealed $SrGa_2S_4:Ce^{3+}$ films prepared at **(a)** 400°C, **(b)** 500°C, **(c)** 600°C respectively. Images in **(d), (e)** and **(f)** show the respective annealed films in vacuum at a temperature of 700°C.

At 400$^{o}$C (Fig 5.3 (a)), the film was smooth with uneven distribution of few spherical particles of different sizes on the surface. After annealing (Fig 5.3 (d)) the surface became rough with increased number of spherical particles on the surface. The smooth surface with steps was observed at 500$^{o}$C as depicted in Fig. 5.3 (b), with few non-uniform cylindrical particles of different sizes. Annealing the film (Fig. 5.3 (e)) resulted in fairly rough surface covered completely with nano-rods like particles. The surface became rough at 600$^{o}$C (Fig. 5.3 (c)), with big particles and after annealing (Fig.5.3 (f)) the roughness and the number of cylindrical particles on the surface layer increased.

Root mean square (rms) values of the unannealed films were measured by AFM. For the film prepared at 400°C with 57 600 number of pulses, the rms value was 16.5 nm while that of the film deposited with 28 800 pulses was 35 nm. It is therefore clear that the surface roughness decreased with increasing number of pulses. This was ascribed to the increase in the thickness of the film's layer as number of pulses were increased, thus improving the film's homogeneity and planarity [5].

### 5.2.4 PHOTOLUMINESCENT PROPERTIES

PL spectra of the unannealed films deposited at different parameters are shown in Figs. 5.4 (a-c).

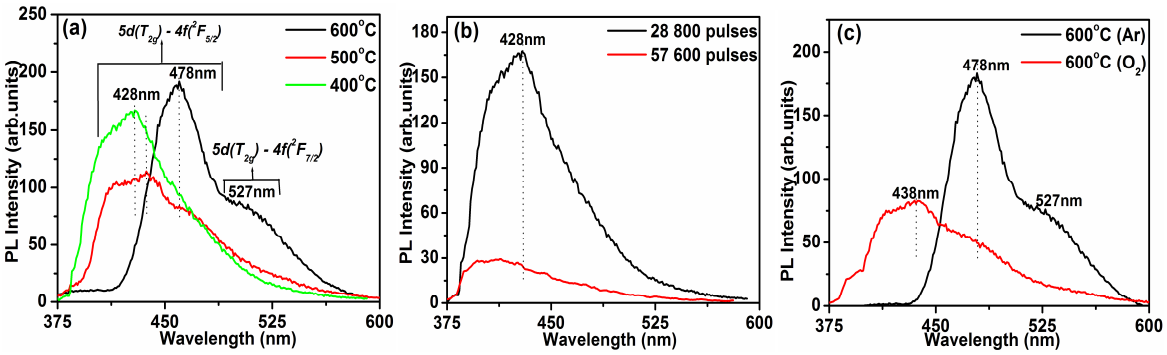


**Fig. 5.4** PL spectra of the as deposited $SrGa_2S_4:Ce^{3+}$ films prepared at **(a)** different substrate temperatures, **(b)** different number of pulses, and **(c)** in Ar and $O_2$ atmospheres.

Shown in Fig. 5.4 (a) are the PL emission spectra for the films deposited at 400, 500 and 600°C respectively. At 400°C, one broad emission band that can be fitted with two Gaussian peaks according to the two $Ce^{3+}$ emission peaks which are known to originate from radiative transitions of the 5d ($T_{2g}$) → 4f ($^2F_{5/2}$) and 5d ($T_{2g}$) → 4f ($^2F_{7/2}$) was observed.

As the substrate temperature was increase to 500°C, a broad band with a small shoulder at approximately 485 nm was observed and a slight shift of the emission peak to the right as indicated in the figure. In addition, the film deposited with $T_{substrate}$ = 400°C was more intense than that deposited with $T_{substrate}$ = 500°C. A further shift to the right was observed from the film deposited at 600°C substrate temperature in Ar atmosphere. The resulting spectrum resembles the $Ce^{3+}$ emission in SrS host [6]. While the possible phases relating to SrS were not detected in the XRD data, the X-ray photoelectron spectroscopy (XPS) data discussed in Chapter 6 (section 6.2.2) confirmed that SrS was formed during the deposition process. SrS was most probably

formed on the film surface from the chemical reaction between the laser ablated $Sr^{2+}$ and $S^{2-}$ species. Note that the well known two emission peaks associated with the crystal field splitting of the $Ce^{3+}$ were clearly resolved and were observed at 478 nm and 527 nm. Similar results were reported elsewhere [7, 8]. Generally, the red-shifting of the emission peaks was simultaneous with increasing substrate temperature. In Fig. 5.4 (b) is the comparison of the PL spectra for the depositions done at 400°C substrate temperature varying number of pulses. One broad peak showing blue emission coming from $Ce^{3+}$ transitions was observed at 28 800 pulses and at 57 600 pulses. A slight shift of the emission peak in comparison to PL at 57 600 pulses as indicated in Fig. 5.4 (b) was observed suggesting the change in bonding of the $SrGa_2S_4:Ce^{3+}$ elements during the preparation of the film. In addition, the film deposited with 28 800 pulses was more intense than that deposited with 57 600 pulses (Fig. 5.4 (b)) as expected from a thicker layer obtained from the increase in the number of pulses.

Fig. 5.4 (c) shows PL spectra for the films deposited in Ar and $O_2$ atmospheres. An intense PL emission was obtained from the film deposited in the Ar gas environment and a less PL emission was observed from the film deposited in $O_2$ gas. Since O is highly reactive, a possibility of a chemical reaction of strontium with oxygen to form non-luminescent SrO layer must be taken into account, thus affecting the stoichiometry near the interface and causing a reduction in the film's PL intensity. This was later confirmed by XPS data discussed in Chapter 6 whereby SrO overlayer was formed when degradation study was performed on the film.

The effects of annealing at 700°C on the PL properties of the films deposited at different substrate temperatures were investigated. Depicted in Figs. 5.5 (a-c) are both unannealed and the annealed PL spectra of the films deposited at different substrate temperatures.

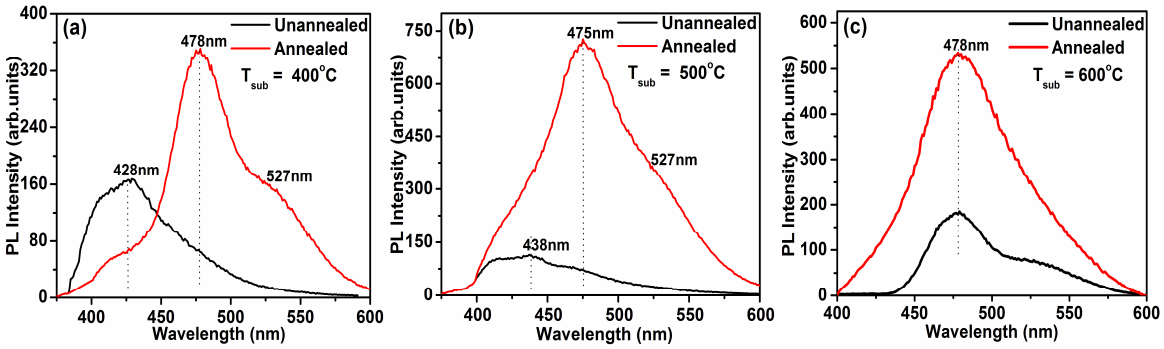


**Fig. 5.5** Unannealed and annealed PL spectra of the $SrGa_2S_4:Ce^{3+}$ films prepared at **(a)** 400°C **(b)** 500°C and **(c)** 600°C.

Annealing films deposited at 400°C and 500°C (Figs. 5.5 (a) and (b)) resulted in the spectra resembling the $Ce^{3+}$ emission in SrS and the PL intensity was increased. At 400°C two resolved peaks at 478 and 527 nm were observed after annealing and at 500°C with the identification of the small and very wide 527 nm peak. The 527 nm shoulder disappeared at 600°C and no further shift was observed at this substrate temperature. A general increase in PL of all annealed films observed can be attributed to the increased roughness of the films observed after annealing in AFM images (Figs. 5.3 (a-c)) with 500°C film giving the highest PL intensity. Note that a shift to red emission was due to the formation of SrS during the deposition process as confirmed by XPS results.

### 5.2.5 CATHODOLUMINESCENT PROPERTIES

In Fig. 5.6, the CL emission spectra for the $SrGa_2S_4:Ce^{3+}$ films deposited at different parameters are shown.

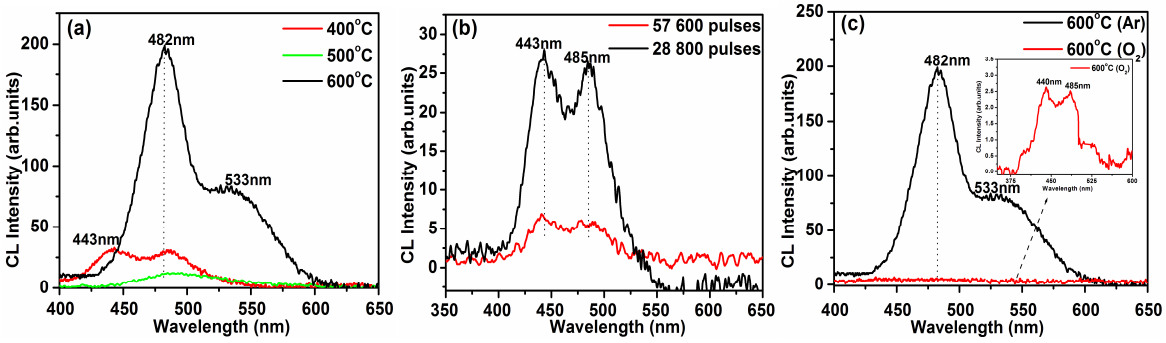


**Fig. 5.6** CL emission spectra of the $SrGa_2S_4:Ce^{3+}$ films deposited at **(a)** various substrate temperature, **(b)** different number of pulses and **(c)** in Ar and $O_2$ atmosphere.

For the film deposited at 400°C in Fig. 5.6 (a), two broad emission peaks around 443 nm and 485 nm which are due to $Ce^{3+}$ radiative transitions were observed. This film exhibited the same pattern as the CL emission of $SrGa_2S_4:Ce^{3+}$ powder phosphor obtained in Chapter 3 (Fig. 3.3 (c)), suggesting a successful stoichiometry transfer of the target material at this substrate temperature. The film (400°C) showed a pure blue CL emission with the peak at the radiative transition 5d ($T_{2g}$) → 4f ($^2F_{7/2}$) being less intense. A low CL intensity was obtained at this substrate temperature due to the low deposition temperature of the substrate. At 500°C one broad peak was observed and two broad peaks around 482 nm and 533 nm at 600°C.

In Fig. 5.6 (b) are the CL emission spectra for different number of pulses. Both the spectra showed two broad peaks around 443 nm and 485 nm according to the $Ce^{3+}$ emission. Shown in Fig. 5.6 (c) are the films for the depositions in different gas atmospheres. For the film prepared in $O_2$, two broad peaks around 440 nm and 485 nm were observed with low CL intensity as in indicated in the inset (Fig. 5.6 (c)). In Ar the film showed SrS:$Ce^{3+}$ emission with relatively higher CL intensity.

Again there was a red-shift of the emission peaks with increasing substrate temperature. Consistent with the PL data, the highest CL intensity was observed from the film deposited with 28 800 pulses as shown in Fig. 5.6 (b). It was again noticed that the film deposited in Ar atmosphere at 600$^{o}$C was more intense than that deposited in $O_2$ atmosphere as shown in Fig. 5.6 (c). The inset of Fig. 5.6 (c) is the stand alone spectrum of the film deposited in $O_2$ showing that the emission spectrum resemble those of the film deposited at a 400$^{o}$C (Fig. 5.6 (a)) and different number of pulses (Fig. 5.6 (b)). From Figs. 5.6 (a-c), it is clear that the high energy excitation by electrons did not bring about a major difference when compared to the PL data in Fig. 5.4 (a-c).

## 5.3 Conclusion

A highly crystalline $SrGa_2S_4$ layer was observed at the growth temperature of 400°C. XRD patterns also showed that the growth of the films is sensitive to substrate temperature. PL and CL showed one broad band that can be fitted with two Gaussian peaks according to the two $Ce^{3+}$ radiative transitions at lower substrate temperatures, low and high pulses and in $O_2$ atmosphere. At high substrate temperature a shift to SrS:$Ce^{3+}$ emission occurred as well as in Ar atmosphere for both UV and high energy electrons excitation. The AFM images before annealing exhibited smooth surface at low substrate temperature, which became rough at high substrate temperature and after annealing in vacuum at 700°C temperature. Non-uniformity in particles of the films and rough surface were observed from the SEM images.

## References

[1] Y Nakanishi, N Uekura, F Nakano and Y Hatanaka, *Journal of Luminescence,* **72-74**, 373-374 (1997).

[2] H Heikkinen, L S Johansson, E Nykänen and L Niinistö, *Applied Surface Science,* **133**, 205-212 (1998).

[3] K Tanaka, Y Inoue, S Okamoto and K Kobayashi, *Journal of Crystal Growth,* **150**, 1211-1214 (1995).

[4] T Yang, B K Wagner, M Chaichimansour, W Park, Z L Wang, and C J Summers, *J. Vac. Sci. Technol. B,* Vol. 14, **No. 3**, May/Jun (1996).

[5] S Christoulakis, M Suchea, N Katsarakis and E Koudoumas, *Appl. Surf. Sci.* **253** 8169-8173 (2007).

[6] V Kumar, S S Pitale S S, M M Biggs, I M Nagpure, O M Ntwaeaborwa and H C Swart, *Mater. Lett.* **64** 752 – 754 (2010)

[7] X Chunxiang, L Zhidong, X Zheng and X Xurong, *Chinese Science. Bulletin,* **43** 7 603-605 (1998).

[8] X Chunxiang, X Zheng, X Xurong and L Zhidong, *Solid State Communications,* **109**, 183-187 (1999).

# CHAPTER 6

# CATHODOLUMINESCENCE DEGRADATION OF $SrGa_2S_4:Ce^{3+}$ THIN FILMS

## Introduction

*It is crucial to obtain a blue emission, high intensity and good colour purity from inorganic electroluminescent (EL) and cathodoluminescent (CL) thin film phosphors for display technology. Most of research has been devoted to the development of such thin film phosphors and high expectations are being place on the $Ce^{3+}$ doped $SrGa_2S_4$ because of its blue emission with good colour purity. In this study $SrGa_2S_4:Ce^{3+}$thin films were prepared by pulsed reactive cross laser ablation (PRCLA). In this chapter, cathodoluminescence degradation, chemical composition, and electronic states of the $SrGa_2S_4:Ce^{3+}$ thin films are reported.*

## 6.1 Experimental

Cathodoluminescence (CL) intensity degradation of $SrGa_2S_4:Ce^{3+}$ thin films were investigated using Auger electron spectroscopy (AES) coupled with the CL spectroscopy. Surface chemical changes were monitored with AES and the light output was measured with a PC2000-UV spectrometer. Primary electron beam current density was typically 12 μA. The Auger and CL data were collected in a vacuum chamber with a base pressure of 7.0 $x10^{-9}$ Torr for the film prepared at $T_{substrate}$ = 400°C and 7.8 x $10^{-9}$ Torr for the $T_{substrate}$ = 600°C film. The films were both deposited with 28 800 number of pulses in Ar environment. Afterwards the chamber was backfilled with oxygen to 1.0 x $10^{-6}$ Torr. The Auger and CL data were collected using the same primary electron beam of 2 keV. The PHI (model 549) Auger spectrometer and S2000 Ocean Optics spectrometer were simultaneously used to collect the Auger and CL data respectively. The decrease of the CL intensities of both films was monitored continuously for a period of 6 hours. The monitored peaks were 443 nm and 485 nm for $T_{substrate}$ = 400°C film and 482 nm and 530 nm for $T_{substrate}$ = 600°C film.

The XPS data were collected before and after degradation to evaluate the chemical composition and electronic states of different elements. The data were collected using the PHI 5000 Versa probe-Scanning ESCA microprobe. $Ar^+$ ion gun with a sputter rate of about 85Å/min was used to minimize charging on the surface when a monochromatic AlKα radiation was used as the excitation source. 25W and 15kV energy x-ray beam of 100μm diameter was used to analyze Sr 3d, O 1s, Ga 2p and S 2p binding energy peaks (pass energy 11eV, analyzer resolution ≤ 0.5eV). Multipak version 8.2 software [1] was used to analyze the chemical elements and their electronic states using Gaussian-Lorentz fits.

## 6.2 Results and Discussions

### 6.2.1 CL INTENSITY DEGRADATION

Fig. 6.1 (a) shows the Auger spectra recorded before and after degradation for the film deposited at 400°C substrate temperature. The degradation pressure was at 1.0 x $10^{-6}$ Torr $O_2$ and the electron beam was accelerated at 2 kV.

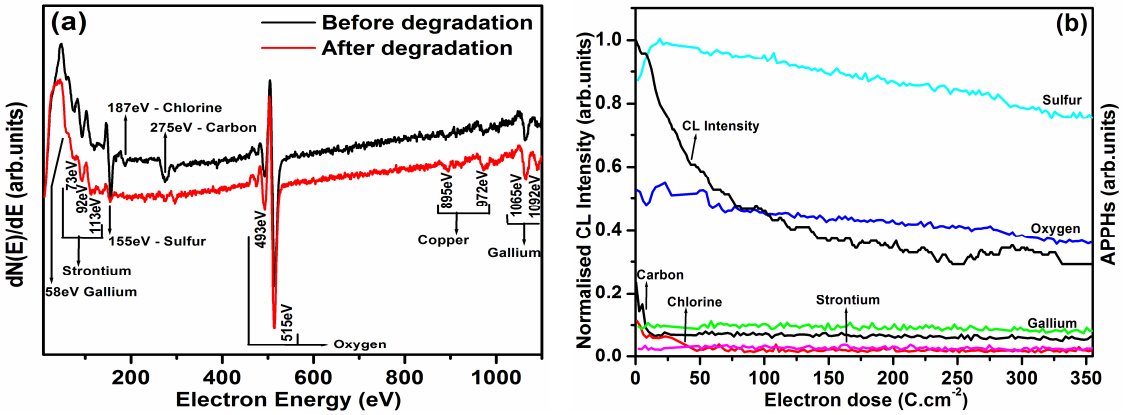


**Fig. 6.1 (a)** Auger and **(b)** APPHs and CL intensity as a function of electron dose spectra of the $SrGa_2S_4:Ce^{3+}$ film deposited with $T_{substrate}$ = 400°C at a pressure of 1.0 x $10^{-6}$ Torr $O_2$ (Electron beam energy = 2keV).

The peak positions of the Auger spectra in Fig. 6.1 (a) before and after degradation are clearly marked. In addition to major elements present in $SrGa_2S_4:Ce^{3+}$ system, chlorine (Cl), oxygen (O) and copper (Cu) peaks were also detected. Cl was probably from precursors used during sample preparation, oxygen was introduced (including a small percentage from the atmosphere) and Cu was from the sample holder. There were no drastic changes in the peak intensity of the sample's major elements (Ga and Sr), except for S peak whose intensity was reduced drastically during the degradation process. Shown in Fig. 6.1 (b) is the Auger peak to peak heights (APPHs) and CL intensity as a function of electron dose of the film deposited at $T_{substrate}$ = 400°C. The trend of the peaks monitored during the degradation process is in agreement with the Auger spectrum shown in Fig. 6.1 (a).

Fig. 6.1 (b) shows an initial increase in S and O Auger peak intensities up to approximately 20 and 70 $C.cm^{-2}$ respectively, and finally the intensity of both peaks decreased with increasing electron dose. C decreased rapidly at the beginning of degradation and thereafter remained constant throughout the degradation process. Ga and Sr peaks were seemingly stable. Note that similar trend of the peaks as that observed at $T_{substrate}$ = 400°C (Fig. 6.1 (b)) film was observed for the $T_{substrate}$ = 600°C film degraded at 1.0 x $10^{-6}$ Torr $O_2$.

Depicted in Fig. 6.2 are the CL intensities as a function of wavelength spectra for measurements taken before and after degradation at 1.0 x $10^{-6}$ Torr $O_2$ for the $T_{substrate}$ = 400°C film and $T_{substrate}$ = 600°C film.

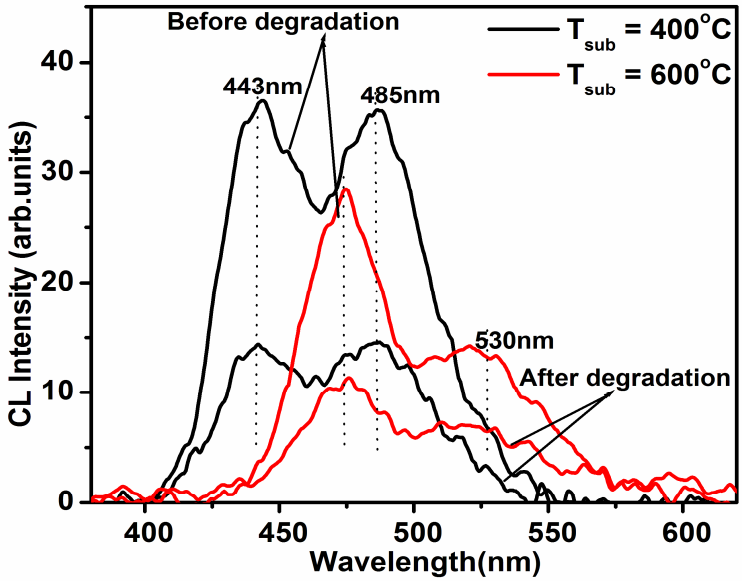


**Fig. 6.2** CL intensity as a function of wavelength spectra of the $SrGa_2S_4:Ce^{3+}$ film deposited at $T_{substrate}$ = 400°C and $T_{substrate}$ = 600°C for the degradation study performed at 1.0 x $10^{-6}$ Torr $O_2$.

The broad emission peaks around 443 nm and 485 nm wavelength for the film deposited at $T_{substrate}$ = 400°C and peaks around 482 nm and 530 nm wavelength for the deposited at $T_{substrate}$ = 600°C which are all due to $Ce^{3+}$ transitions were observed. The $Ce^{3+}$ emission in $SrGa_2S_4$ lies at a shorter wavelength than in SrS [2], therefore, a high CL intensity with pure blue emission was observed for the film deposited at $T_{substrate}$ = 400°C. Nevertheless, a significant decrease in the CL intensity was observed from both films.

The effects of different oxygen pressures were investigated on the degradation characteristics of the films. Shown in Figs. 6.3 (a) and (b) are the normalized CL intensity curves of $T_{substrate}$ = 400°C and $T_{substrate}$ = 600°C films at oxygen pressure of 1.0 x $10^{-6}$ Torr and base pressure 7.8 x $10^{-9}$ Torr. The results exhibited a rapid decrease of CL intensity for $T_{substrate}$ = 600°C film at both pressures as compared to $T_{substrate}$ = 400°C film. Generally, the rate of degradation of CL intensity was faster when the chamber was backfilled with oxygen. Again at this pressure, the fastest degradation for $T_{substrate}$ = 600°C film was observed, suggesting a different nature of reactions on the surface which are explained by the XPS in the next section.

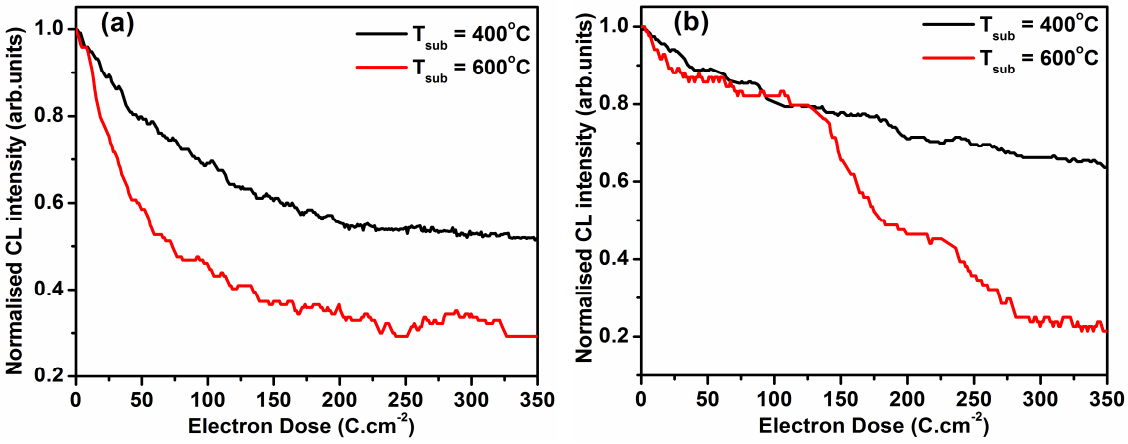


**Fig. 6.3** Normalized CL intensity as a function of electron dose of the $SrGa_2S_4:Ce^{3+}$ films degraded at **(a)** 1.0 x $10^{-6}$ Torr $O_2$ and **(b)** 7.8 x $10^{-9}$ Torr base pressure.

The same sequences of degradation curves observed for each element in Fig. 6.1 (b) were also observed on the degradation of the powder at 1.0 x $10^{-6}$ Torr $O_2$ pressure in Chapter 4 (Fig. 4.2 (b)). Thus, C peak was observed to be decreasing at a faster rate, stimulating surface chemical reactions which resulted in the rapid decrease of the degradation of CL intensity for $T_{substrate}$ = 600°C film at this pressure. The other factor might be the formation of SrS that occurred during the deposition $SrGa_2S_4:Ce^{3+}$ film at this substrate temperature giving CL emission of $SrS:Ce^{3+}$. K. Takahashi et al [3] reported on possible degradation mechanisms for the SrS:Ce electroluminescence (EL). They concluded that the degradation of SrS:Ce EL is induced by $Sr^{2+}$ lattice vacancies which cause ionic conduction.

Cathodoluminescence (CL) as a function of wavelength spectra for the film deposited at $T_{substrate}$ = 400°C were also recorded at different accelerating voltages (1.5 – 2.5 kV) and measurements were taken with the chamber at 7.0 x $10^{-9}$ Torr pressure. Shown in Fig. 6.4 is the CL intensity as a function of wavelength spectra for the $T_{substrate}$ = 400°C film at different accelerating voltages. Two broad peaks were observed as explained above and CL intensity was increasing with an increase in the beam voltage. Similar results were observed from the powder in Chapter 4 (Fig. 4.4 (a).

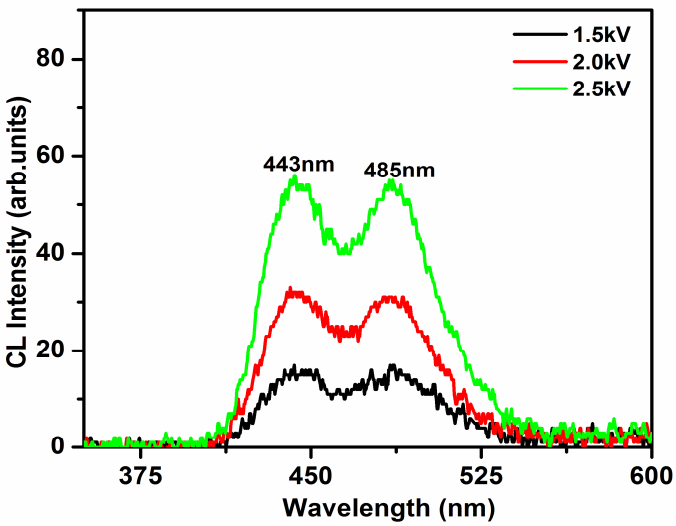


**Fig. 6.4** CL intensity as a function of wavelength spectra of the $SrGa_2S_4:Ce^{3+}$ film deposited at $T_{substrate}$ = 400°C with measurements recorded at different accelerating voltages.

### 6.2.2 XPS

X-ray photoelectron spectroscopy (XPS) was used to analyze the chemical state of the elements present in $SrGa_2S_4$ host matrix. Shown in Fig. 6.5 are the XPS survey spectra for both undegraded and degraded spot for the film deposited at 600°C in Ar environment. The spectra confirmed the presence of the major elements, namely, Sr, Ga and S suggesting a successful deposition of $SrGa_2S_4$ at this substrate temperature.

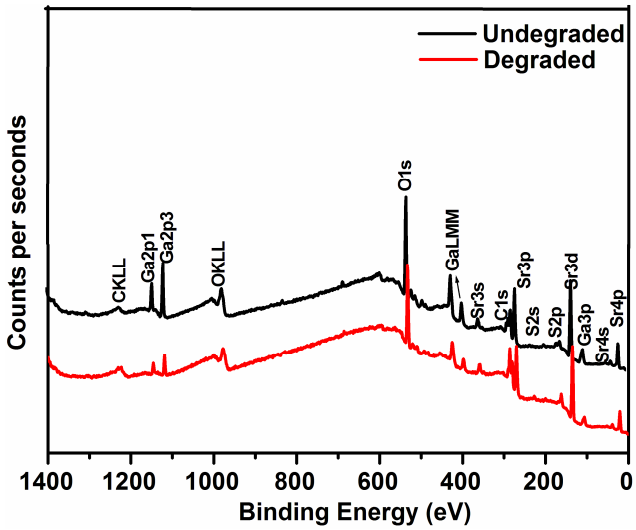


**Fig. 6.5** XPS survey spectra of the undegraded and degraded spots for the film deposited at $T_{substrate}$ = 600°C.

Depicted in Fig. 6.6 are the high resolution XPS spectrums of Sr, Ga, and S before (a-c) and after (d-f) degradation at 1.0 x $10^{-6}$ Torr $O_2$.

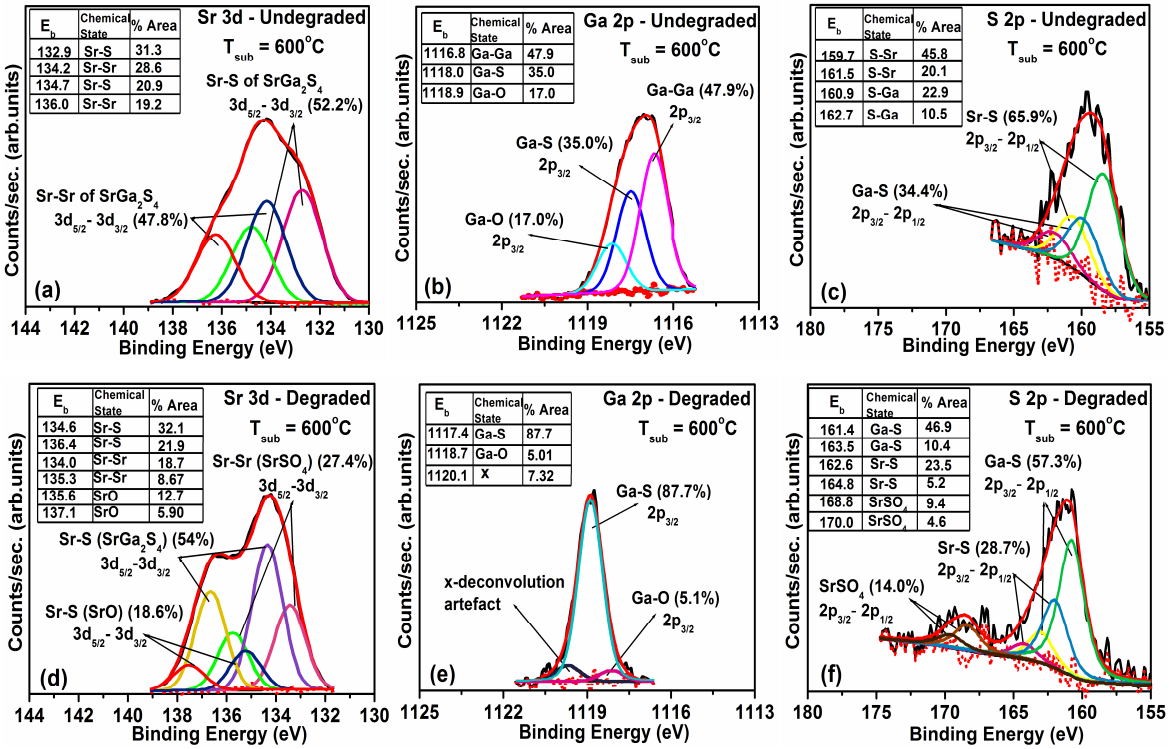


**Figs. 6.6 (a-f)** XPS high resolution scans and fitting results for (a, b & c) undegraded regions (before ageing) and (d, e & f) degraded (after ageing) regions of the $SrGa_2S_4:Ce^{3+}$ phosphor film deposited at $T_{substrate}$ = 600°C.

Fig. 6.6 (a) shows the Sr 3d fitted peaks for the undegraded spot at positions $3d_{3/2}$ and $3d_{5/2}$ corresponding to the Sr-S and Sr-Sr and/or $SrSO_4$ bonds in $SrGa_2S_4$. Two additional peaks were detected after degradation signifying the formation of Sr-O containing species, and were identified as SrO peaks as shown in Fig. 6.6 (d). The binding energies are shown in the inset tables.

Shown in Figs. 6.6 (b) and (e) are the $2p_{3/2}$ Ga peaks before and after degradation. Before the film was exposed to the beam of electrons, Ga $2p_{3/2}$ XPS spectrum is comprised of three components, namely, Ga-S, Ga-O and Ga-Ga bonds corresponding to the metallic Ga, $Ga_2O_3$ and $Ga_2S_3$. A large contribution from Ga-Ga bond (47.9%) suggests that there is Ga rich region in the film. Due to the electron beam irradiation, the bond between Ga and Ga was broken resulting in the enlargement of the $Ga_2S_3$ peak and minimizing the $Ga_2O_3$ peak after degradation.

The appearance of another peak at the energy of 1120.1 eV was the deconvolution artefact that does not correspond to any chemical compound as explained by C Sanz et al [4] in the XPS analysis of the gallium sulfide thin film.

In Fig. 6.6 (c) is the fitted S 2p XPS spectrum for the undegraded spot on the film. Before degradation, the spectrum has two components of Ga-S and Sr-S bonds at positions $2p_{1/2}$ and $2p_{3/2}$ corresponding to gallium sulfide and strontium sulfide with bigger contribution coming from the Sr-S bond. Their respective binding energies are shown in the figure. After degradation an appearance of $SrSO_4$ peaks were observed at 168.8 and 170 eV. The oxides layers formed on the surface after degradation are believed to have contributed to the fast degradation of $T_{substrate}$ = 600$^o$C film at 1.0 x $10^{-6}$ Torr $O_2$ pressure.

## 6.3 Conclusion

The XPS and AES were employed to study the effects of various oxygen pressures on the degradation characteristics of $SrGa_2S_4:Ce^{3+}$ thin film prepared at 400$^o$C and 600$^o$C substrate temperatures. The rate of degradation was slower at 7.0 x $10^{-9}$ Torr base pressure for $T_{substrate}$ = 400$^o$C film and CL intensity increased with an increase in the electron beam voltage. At 1.0 x $10^{-6}$ Torr $O_2$ pressure, the rate of the CL intensity degradation decreased rapidly for both films deposited at $T_{substrate}$ = 400$^o$C and $T_{substrate}$ = 600$^o$C. Auger results showed decrease in S content at all pressures and O was increasing in content at base pressure and decreasing at 1.0 x $10^{-6}$ Torr $O_2$ pressures. The films exposure to beam of electrons resulted in the formation of SrO, $SrSO_4$ and $Ga_2O_3$ compounds on the surface after degradation as confirmed by XPS.

## References

[1] F Moulder, W F Stickle, P E Sobol and K D Bomben, *Handbook of X-ray Photoelectron Spectroscopy, ULVAC-PHI, Inc, 370 Enzo,* Chigasaki 253-8522, Japan (1995).

[2] K Tanaka, Y Inoue, S Okamoto, K Kobayishi and K Takizawa, *Jpn. J. Appl. Phys.* Vol **38**, pp 3517-3521 (1997).

[3] K Takahashi, K Shibuya and A Kondo, *Journal of Crystal Growth,* **117**, 979-982 (1992).

[4] C Sanz, C Guillén and M J Guitiérrez, *J. Phys. D: Appl. Phys.* **42**, 085108, pp 6 (2009).

# CHAPTER 7

# SUMMARY AND CONCLUSION

## Introduction

*Strontium thiogallate doped with $Ce^{3+}$ has been widely studied. The CL intensity degradation of $Ce^{3+}$/ $Eu^{2+}$ activated $SrGa_2S_4$ has been reported earlier [1], the ageing mechanism and the identification of surface chemical changes that occurs with increasing Coulomb dose has not yet been sufficiently investigated using surface sensitive techniques. In the work presented in this thesis, surface chemistry variations of $SrGa_2S_4:Ce^{3+}$ powder phosphors were investigated and the possible mechanism of CL intensity degradation was discussed. In addition to this work, $SrGa_2S_4:Ce^{3+}$ thin films were prepared for the first time by pulsed reactive cross laser ablation (PRCLA). Basically, this chapter gives a summary on the work covered in this dissertation. That is, the study on cathodoluminescence degradation and surface characterization of $SrGa_2S_4:Ce^{3+}$ powder and thin films. It also gives a summary of possible work for future investigation based on the same phosphor.*

## 7.1 THESIS SUMMARY

In this study, commercial $SrGa_2S_4:Ce^{3+}$ powder phosphor and the pulsed reactive cross laser ablated thin films were characterized. The Lambda Physik EMG 203 MSC 309 nm XeCl excimer laser was used to ablate the $SrGa_2S_4:Ce^{3+}$ pellet. Characterization of both the powder and thin films was carried out using different techniques. For investigation of optical properties, PL and CL data were collected with Varian Cary Eclipse Fluorescence Spectrophotometer and S2000 Ocean Optics Spectrometer respectively. The XRD was used for structural analysis.

To study morphology and the composition of the $SrGa_2S_4:Ce^{3+}$ powder phosphor, SEM coupled with EDS were employed. Morphological and topographical analyses of the films were examined by SEM and AFM respectively. Absorption measurements were also collected from the powder only. Cathodoluminescence intensity degradation studies for both films and powder were performed. AES was used to monitor the elemental surface changes and XPS to analyze the electronic state of the elements present in the $SrGa_2S_4:Ce^{3+}$ powder phosphor before and after a prolonged irradiation to high energy electrons.

The $SrGa_2S_4:Ce^{3+}$ powder was successfully characterized. The diffraction peaks associated with orthorhombic structure of $SrGa_2S_4$ were obtained and found to correspond well with the JCPDS (77-1189) standard data. Both PL and CL showed two broad peaks around 444 nm and 485 nm which are known to originate from radiative $Ce^{3+}$ transitions. However, a substantial broadening was observed in the emission spectra from cathode excitation versus photo-excitation and was associated with the known sensitivity to the surrounding ligands of the 5d state of $Ce^{3+}$ which is directly exposed to the local environment. This behavior is usually observed within the host matrix band-gap. A change in the intensity ratio of the emission spectra was also observed and was attributed to the electron-hole recombination process taking place within the band gap of the host ($SrGa_2S_4$) during its interaction with UV and electrons beams. $SrGa_2S_4:Ce^{3+}$ phosphor was found to absorb around 300 nm and this result is in line with the literature. SEM images exhibited irregular shapes of unevenly distributed particles and EDS confirmed the presence of major elements.

The present study presented work on $Ce^{3+}$ activated $SrGa_2S_4$ films prepared for the first time using pulsed reactive cross laser ablation. During the preparation of the films, the substrate temperature, number of pulses and working pressure are the parameters that were varied. A shift to SrS emission was observed from the films deposited at the substrate temperatures of 500 and 600$^o$C for CL and at 600$^o$C for PL. The CL spectrum for the film deposited at 400$^o$C resembles that of the commercial powder.

The film deposited at higher number of pulses gave better PL than the one deposited at low number of pulses. The deposition performed in oxygen atmosphere showed relatively weak CL and PL emission. This was ascribed to O iso-electronic traps in the near surface region [2].

The XRD results of the films grown at a substrate temperature of 400$^o$C showed a highly crystalline $SrGa_2S_4$ layer. However, the peaks corresponding to Si were identified. The results suggest an admixture of Si and $SrGa_2S_4$ on the surface layer during ablation. An increase of the substrate temperature to 500$^o$C and 600$^o$C resulted in conspicuous peaks observed along the orientation (0 6 2). At low and high number of pulses, similar XRD patterns were obtained with the main peaks of SrGa2S4 along the orientation (0 6 2), (4 2 2) and (4 0 4) giving poor crystallinity at higher number of pulses. Similar results obtained at higher number of pulses were observed for the film deposited in oxygen atmosphere.

SEM images showed smooth surface with small and big particles not uniformly distributed on the surface for all films deposited at different conditions. AFM exhibited smooth surface at lower substrate temperature and the surface became rough as substrate temperature was increased. Rougher surface was observed after annealing the films in vacuum. Generally surface roughness increased as substrate temperature was increased and these results were confirmed by the measurements of the root mean square values. Increasing number of pulses during deposition resulted in the decrease in the surface roughness. Roughness was observed to decrease when the deposition was performed in Ar to $O_2$ atmosphere.

The Auger spectra taken before and after degradation for both films and powder showed the presence of the major elements, that is , Sr, Ga and S. Additional elements such as Cl, O and Cu were also detected. CL was believed to be coming from precursors, O from the atmosphere and Cu from the sample holder.

The Auger peak to peak height(s) spectra showed increase in O Auger peak intensity for degradation carried out at base pressures ($1.3 \times 10^{-8}$ or $7.0 \times 10^{-9}$ Torr) and decreasing at oxygen pressure ($1.0 \times 10^{-6}$ Torr $O_2$) for both powders and films. S and C peak intensities were decreasing and no significant changes were observed from Sr and Ga Auger peaks.

The results from RGA revealed the $N_2$ and $O_2$ gases dominating the vacuum chamber together with traces of $H_2$, $H_2O$, CO and $CO_2$ species. According to ESSCR, dissociated surface-physisorbed molecular species (e.g. $H_2O$, $H_2$ or $O_2$) by the electron beam are converted to reactive atomic hydrogen and oxygen, which react with S and C on the surface. Subsequently, volatile sulfur and carbon compounds such as $SO_x$ or $H_2S$, CO or $CO_2$ are formed and which desorbed from the surface.

The XPS high resolution scans of Sr, S and Ga before and after electron beam irradiation were fitted. Degraded spots of both powders and thin films were shown to contain phases associated with SrO, $SrSO_4$ and $Ga_2O_3$ layers on the surface. The formation of these layers was explained according to the electron stimulated surface chemical reaction (ESSCR) model. It was speculated that these layers contribute to the CL intensity degradation.

## 7.2 FUTURE WORK

$SrGa_2S_4$: $Ce^{3+}$ thin films were prepared varying different parameters utilizing the PRCLA technique in this study. However, a wide range of deposition conditions were not covered. The effects of parameters such as working atmosphere, a wide range of substrate temperature, and laser frequency must be investigated.

## References

[1] C.Y. Duan, J. Chen, S.Z. Deng, N.S. Xu, J.H. Zhang, H.B. Liang, Q. Su. J. Vac. Sci. and 33333+Technol. B: Micro. and Nano. Struct., 25 (2007) 618.

[2] J.S. Sebastian, H.C. Swart, T.A. Trottier, S.L. Jones, and P.H. Holloway, J. Vac. Sci. Technol. A **15** (4), (1997) 2349.

**Publications**

- P A Moleme, Shreyas S Pitale, H C Swart and O M Ntwaeaborwa, Investigation on ageing characteristics and identification of surface chemical changes on $SrGa_2S_4:Ce^{3+}$ display phosphor under electron beam bombardment. **Accepted July 2011**

- P A Moleme, H C swart and O M Ntwaeaborwa, Optical properties of $SrGa_2S_4:Ce^{3+}$ thin films prepared by pulsed reactive cross laser ablation (PRCLA) technique. **Submitted July 2011**

**Conferences**

- P A Moleme, O M Ntwaeaborwa and H C Swart, Cathodoluminescence degradation of $SrGa_2S_4:Ce^{3+}$ phosphor powder.

  $55^{th}$ Annual Conference of the South African Institute of Physics (SAIP), hosted by CSIR NLC, Pretoria, 27 September – 01 October 2010.

- P A Moleme, O M Ntwaeaborwa and H C Swart, Optical properties of $SrGa_2S_4:Ce^{3+}$ thin films prepared by Pulse Reactive Cross Laser Ablation (PRCLA) technigue.

  $56^{th}$ Annual Conference of the South African Institute of Physics (SAIP), hosted by UNISA, St Georges Hotel and Convention Centre, Pretoria, 12 – 15 July 2011.

- P A Moleme, S S Pitale, O M Ntwaeaborwa and H C Swart, Investigation on ageing characteristics and identification of surface chemical changes on $SrGa_2S_4:Ce^{3+}$ display phosphor under electron beam bombardment.

  $4^{th}$ South African Conference on Photonic Material, hosted by UFS, Kariega Game Reserve, 2 – 6 May 2011.